Pflugers Arch - Eur J Physiol (2013) 465:1261–1279
DOI 10.1007/s00424-013-1261-9



# Conferring electrogenicity to the electroneutral phosphate cotransporter NaPi-IIc (SLC34A3) reveals an internal cation release step

**Monica Patti · Chiara Ghezzi · Ian C. Forster**

Received: 19 December 2012 / Revised: 14 February 2013 / Accepted: 4 March 2013 / Published online: 21 March 2013


**Abstract** The SLC34 family of $Na^+$-dependent inorganic phosphate cotransporters comprises two electrogenic isoforms (NaPi-IIa, NaPi-IIb) and an electroneutral isoform (NaPi-IIc). Both fulfill essential physiological roles in mammalian phosphate homeostasis. By substitution of three conserved amino acids, found in all electrogenic isoforms, at corresponding sites in NaPi-IIc, electrogenicity was re-established and the $Na^+/P_i$ stoichiometry increased from 2:1 to 3:1. However, this engineered electrogenic construct (AAD-IIc) had a reduced apparent $P_i$ affinity and different presteady-state kinetics from the wild-type NaPi-IIa/b. We investigated AAD-IIc using electrophysiology and voltage clamp fluorometry to elucidate the compromised behavior. The activation energy for cotransport was threefold higher than for NaPi-IIc and 1.5-fold higher than for NaPi-IIa and the temperature dependence of presteady-state charge displacements suggested that the large activation energy was associated with the empty carrier reorientation. AAD-IIc shows a weak interaction of external $Na^+$ ions with the electric field, and thus retains the electroneutral cooperative interaction of two $Na^+$ ions preceding external $P_i$ binding of NaPi-IIc. Most of the presteady-state charge movement was accounted for by the empty carrier (in the absence of external $P_i$), and the cytosolic release of one $Na^+$ ion (in the presence of $P_i$). Simulations using a kinetic model recapitulated the presteady-state and steady-state behavior and allowed identification of two critical partial reactions: the final release of $Na^+$ to the cytosol and external $P_i$ binding. Fluorometric recordings from AAD-IIc mutants with Cys substituted at functionally important sites established that AAD-IIc undergoes substrate- and voltage-dependent conformational changes that correlated qualitatively with its presteady-state kinetics.

**Keywords** Phosphate cotransport · Electrophysiology · Voltage clamp fluorometry · Presteady state · Steady state · Activation energy

## Introduction

Type II sodium/phosphate cotransporters (NaPi-II) catalyze transport of inorganic phosphate ($P_i$) using the transmembrane $Na^+$ electrochemical gradient. They belong to the SLC34 family of solute carriers (www.bioparadigms.com) [15] that preferentially transport divalent $P_i$ ($HPO_4^{2-}$) [17]. The family comprises three isoforms to which all currently identified members have been assigned according to their genetic pedigree, molecular features, and tissue localization: the electrogenic NaPi-IIa and electroneutral NaPi-IIc are localized exclusively in the renal proximal tubule and the electrogenic NaPi-IIb is expressed in nonrenal, epithelial-like tissues. The difference between the electrogenic and electroneutral isoforms is reflected in their $Na^+$–$P_i$ cotransport stoichiometries: NaPi-IIa,b (SLC34A1, A2) have a 3:1 stoichiometry [17] and translocate one net charge per transport cycle; NaPi-IIc (SLC34A3) has a 2:1 stoichiometry with no detectable net charge translocation. The electrogenic and electroneutral cotransport mechanisms can be understood in terms of a kinetic scheme (Fig. 1a) that describes their respective transport cycles as an ordered sequence of partial reactions, some of which have been identified experimentally. For example, electrogenicity can be accounted for by assigning charge displacement to the empty carrier (0↔1) together with extra- and

Monica Patti and Chiara Ghezzi contributed equally to this work.

M. Patti · C. Ghezzi · I. C. Forster (✉)
Institute of Physiology and Zurich Center for Integrative Human Physiology (ZIHP), University of Zurich, Winterthurerstrasse 190, 8057 Zurich, Switzerland
e-mail: iforster@access.uzh.ch

intracellular interactions of one $Na^+$ ion (1↔2, 0↔9) [2, 13, 19]. This cation is postulated to account for the uncoupled leak [2]. To reconcile this model with electroneutral cotransport mediated by SLC34A3 (NaPi-IIc), the scheme was modified (*shaded area*, Fig. 1a), based on the interpretation of fluorometric assays [20]. For NaPi-IIc, 2 $Na^+$ ions are assumed to interact with the protein before $P_i$, but unlike NaPi-IIa/b, only one of these cations contributes to net transport. We postulated that the first $Na^+$ ion to interact with NaPi-IIc acts as a "catalytic activator" for cotransport [20] that gives rise to cooperative binding of a 2nd $Na^+$ ion before $P_i$ binds (2↔3). This first $Na^+$ ion would remain bound during the cotransport cycle, but contributes neither to net coupled transport nor leak, which in the case of NaPi-IIc is undetectable [4]. Thus, for the electrogenic isoforms both leak and cotransport modes involve the translocation of one net positive charge between the external and internal milieus, and both involve an electroneutral intrinsic translocation of substrate (transitions 2↔9 and 5↔6, respectively).

Apart from electrogenicity and leak, other kinetic properties (apparent substrate affinities, pH dependence) are essentially the same for the electrogenic and electroneutral isoforms [13, 31, 33]. These common functional properties accord with the finding that SLC34 proteins display an overall amino acid similarity of ≈57 %. This is even greater in the predicted transmembrane domain regions [36] and therefore all isoforms most likely share a common 3-D structure. The current lack of a 3-D structure and apparent absence of homology with membrane transport proteins with resolved structures has necessitated using indirect approaches (mutagenesis, cysteine scanning, and crosslinking) to determine the structure–function relationships [16, 19, 20].

It is noteworthy that small differences in the amino acid sequence in SLC34 proteins can lead to significant functional changes in pH sensitivity [9] and electrogenicity [4]. In the latter case, we identified a trio of amino acids (Ala-218, Ala-220, Asp-224, mouse NaPi-IIa sequence numbering), located in a putative linker region between two predicted α-helical transmembrane domains (TMD4 and 5, Fig. 1b), which were shown to be critical for electrogenic behavior. A comparison of the sequences of the electrogenic isoforms from a number of species reveals that the Ala-Ala-Asp trio is conserved. In the electroneutral isoforms, these are replaced with a Ser-Ser-Gly trio (Fig. 1b, inset). If the Ala-Ala-Asp trio was substituted at the equivalent sites in the electroneutral NaPi-IIc (Ser-189, Ser-191, Gly-195) electrogenicity was re-established, as evidenced by robust $P_i$-induced steady-state currents, presteady-state relaxations and the predicted 3:1 stoichiometry [4], all of which are hallmarks of electrogenic SLC34 proteins. Moreover, the replacement of the critical aspartic acid in NaPi-IIa with a glycine resulted in electroneutral cotransport [32]. However, the molecular engineering of NaPi-IIc resulted in compromised cotransport kinetics. The modified protein (hereafter referred to as AAD-IIc) showed a >200-fold reduced apparent affinity for $P_i$: the Michaelis constant ($K_{0.5}^{Pi}$) was >1 mM (compared with ≈0.06 mM for NaPi-IIc), whereas for $Na^+$ activation (1 mM $P_i$), the apparent affinity constant ($K_{0.5}^{Na}$) ≈80 mM was only marginally affected (≈40 mM for NaPi-IIc) [19]. Furthermore, compared with other electrogenic isoforms, the presteady-state charge movements appeared to show little dependence on external [$Na^+$] (e.g., [2, 33]). These deviations from expected behavior suggested that other differences in the respective amino acid sequences were also important determinants of the AAD-IIc kinetic profile.

This study focuses on the identification of partial reactions in the SLC34 cotransport cycle (Fig. 1a) that confer the unique behavior of AAD-IIc. By combining presteady-state analysis and voltage clamp fluorometry (VCF) under conditions where the state occupancy of AAD-IIc can be readily defined, we could relate these partial reactions to specific voltage- and substrate-dependent conformational changes of the protein. Our findings offer new insights into how membrane voltage is transduced by cation-driven transporters and provide compelling evidence that the final step in substrate release to the cytosol involves the release of a single $Na^+$ ion.

## Methods

### Solutions and reagents

Standard extracellular solution (100Na) contained (in millimolar): 100 NaCl, 2 KCl, 1.0 $MgCl_2$, 1.8 $CaCl_2$, 10 HEPES, pH 7.4 adjusted with TRIS base. In $Na^+$ substitution experiments, NaCl was equimolarly replaced with choline Cl (100Ch) and solutions with intermediate [$Na^+$] were obtained by mixing 100Na with 100Ch in appropriate portions to maintain a constant molarity. $P_i$ was added from a 1 M $K_2HPO_4/KH_2PO_4$ stock premixed to give pH 7.4. Modified Barth's solution for storing oocytes contained (in in millimolar): 88 NaCl, 1 KCl, 0.41 $CaCl_2$, 0.82 $MgSO_4$, 2.5 $NaHCO_3$, 2 $Ca(NO_3)_2$, 7.5 HEPES, pH 7.5 adjusted with Tris and supplemented with 5 mg/l doxycyclin and 5 mg/l gentamicin. All standard reagents were obtained from either Sigma-Aldrich or Fluka (Buchs, Switzerland). 2-(Trimethylammonium) ethylmethanethiosulfonate bromide (MTSET) and 2-aminoethyl methanethiosulfonate (MTSEA) were obtained from Toronto Research Chemicals or Biotium (USA); 2-((5(6)-tetramethylrhodamine)carboxylamino) ethyl methanethiosulfonate (MTS-TAMRA) was obtained from Biotium (USA).

### Site-directed mutagnesis and cRNA preparation

cDNA encoding wild-type (WT) mouse NaPi-IIc (GenBank/EMBL/DDBJ accession n. AB054999) was subcloned into a plasmid (pT7T3D-Pac, a kind gift from K.-I. Miyamoto,

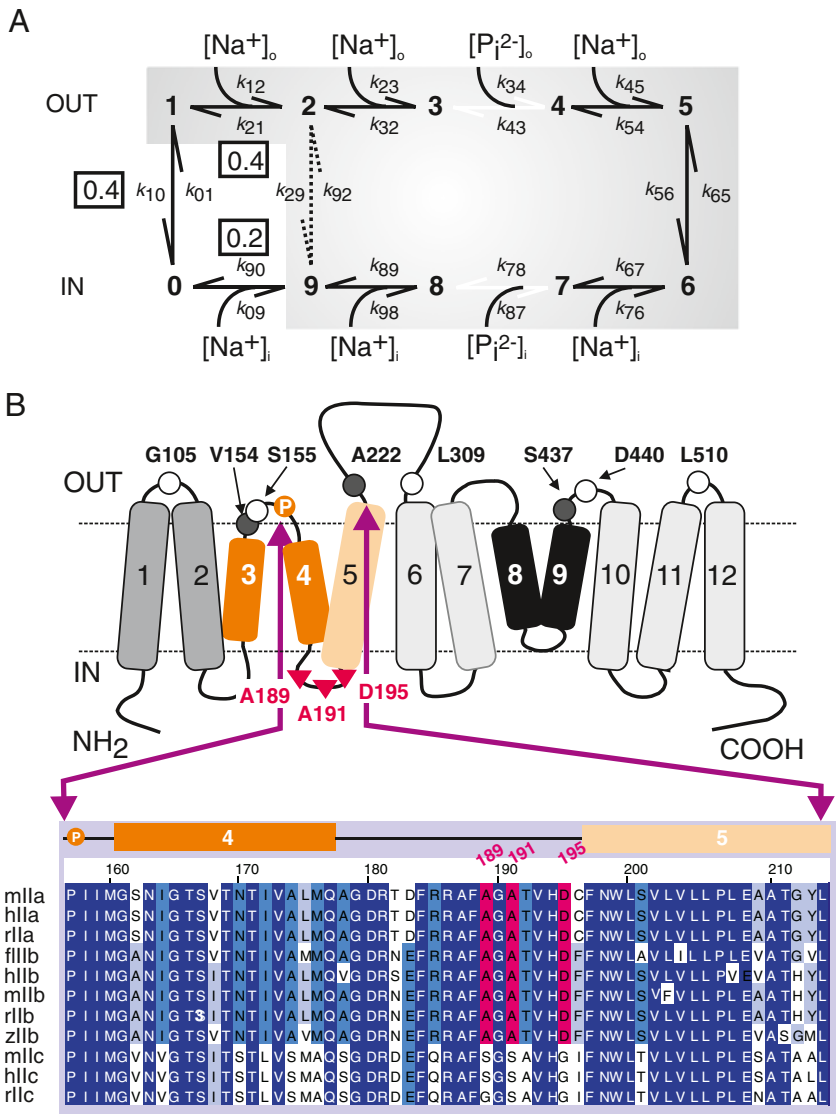


**Fig. 1** SLC34 protein structure-function background. **a** A 10-state kinetic scheme for SLC34 proteins describes the electrogenic transport cycle. *Shaded* states and associated transitions are postulated to be occur in the electroneutral NaPi-IIc transport cycle (see [20]). *Boxed values* indicate effective valence associated with three partial reactions for the electrogenic NaPi-IIa/b. Transition (2↔9) accounts for uncoupled $Na^+$ leak (see [1]). The empty carrier is assumed to occupy one of two states ("inward" or "outward" oriented), transitions between which involve the movement of an equivalent $0.4e^-$ across the transmembrane electric field. Hyperpolarizing potentials increase the probability of occupancy of state 1, which allows the sequential binding of two $Na^+$ ions to their respective binding sites within the transmembrane electric field and is equivalent to $0.4e^-$ moving across the transmembrane electric field. This is followed by binding of $HPO_4^{2-}$ and a third $Na^+$ to form an electroneutral complex followed by substrate translocation. Substrate release to the cytosol is also assumed to be ordered. The final release of the third $Na^+$ ion is modeled as a weakly voltage dependent ($0.2e^-$ equivalent charge) transition that leaves the protein in an "inward" oriented empty carrier state (state 0) and a reorientation to state 1 occurs under the influence of the transmembrane electric field. **b** Secondary topology model showing the three sites in NaPi-IIc critical for restoring electrogenicity to form the AAD-IIc construct (*triangles*). For Cys mutagenesis of AAD-IIc, cysteines were substituted individually at sites predicted to be externally accessible (*circles*). Sites that were labeled with a fluorophore, as evidenced by resolvable voltage-dependent changes in fluorescence, are indicated (*filled circles*). Sites were selected to correspond to previous data obtained from Cys mutagenesis studies of SLC34 isoforms (see Table 1). Inset shows the sequence alignment for the indicated region to emphasize the high degree of identity in the predicted transmembrane domain regions and the lack of charge at site 195 for the electroneutral NaPi-IIc. Abbreviations for species prefixes: *f* flounder, *h* human, *m* mouse, *r* rat, *z* zebra fish. Numbering according to mouse NaPi-IIc sequence

Tokushima University, Tokushima, Japan). Novel cysteines were introduced using the Quickchange site-directed mutagenesis kit (Stratagene Inc., La Jolla, CA, USA) into the AAD-IIc protein at the following sites according to the mouse NaPi-IIc sequence numbering (new mutant name in parenthesis): Gly-105 (AAD-IIc-105), Val-154 (AAD-IIc-154), Ser-155 (AAD-IIc-155), Ala-222 (AAD-IIc-222), Leu-309 (AAD-IIc-309), Ser-437 (AAD-IIc-437), Asp-440 (AAD-IIc-440), and Leu-510 (AAD-IIc-510). The sequence was verified by sequencing (Microsynth, Switzerland), linearized with *NotI* and cRNA was

synthesized in the presence of Cap analog using the T7 Message Machine kit (Ambion, Inc., Austin, TX, USA).

### Expression in *Xenopus laevis* oocytes

Female *X. laevis* frogs were purchased from *Xenopus* Express (France). Portions of ovaries were surgically removed from frogs anesthetized in MS222 (tricaine methansulphonate) and cut in small pieces. Oocytes were treated for 45 min with collagenase (crude type 1A) 1 mg/ml in 100Na solution (without $Ca^{2+}$) in presence of 0.1 mg/ml trypsin inhibitor type III-O. Healthy stage V-VI oocytes were selected, maintained in modified Barth's solution at 16 °C, and injected with 10 ng of cRNA. Experiments were performed 4–7 days after injection. All animal procedures were conducted in accordance with the Swiss Cantonal and Federal legislation relating to animal experimentation.

### Two-electrode voltage clamp

All voltage clamp experiments were performed using a two-electrode voltage clamp (TEC-10CX, NPI, Tamm, Germany). Oocytes were impaled with microelectrodes filled with 3 M KCl, with a typical resistance of <1 MΩ [13, 18]. The temperature of the recording chamber was monitored using a thermistor probe (TS-2, NPI, Tamm, Germany) placed close to the oocyte. The temperature of the recording chamber and incoming superfusate were regulated using Peltier cooling elements driven by a continuous feedback controller (TC-10, NPI Tamm, Germany). Data acquisition was performed using a 1440 Digidata (Molecular Devices Corp, USA). For recordings at constant holding potential, currents were acquired at >20 samples/s and filtered at 10 Hz. Faster sampling rates (up to 20 k samples/s) were used for voltage step recordings with filtering (digital and analog) adjusted accordingly.

Steady-state currents were obtained using a protocol in which membrane voltage steps were made from the holding potential ($V_h$)=−60 mV, to test voltages in the range −180 to +80 mV in 20 mV increments. The steady-state $P_i$-dependent current ($I_{Pi}$) was obtained by subtracting control traces (in 100Na solution) from the corresponding traces in the presence of $P_i$. The current was measured in a region where all presteady-state relaxations were completed. Data was rejected if contaminated by endogenous $Cl^-$ currents. Steady state $P_i$ activation was determined by varying the $P_i$ concentration in presence of 100Na and subtracting the respective currents in 100Na from those in 100Na+$P_i$. $I_{Pi}$ were fit with a form of the modified Hill equation:

$$I_{Pi} = I_{Pi}^{\max}\left([S]^{n_H}/\left([S]^{n_H} + \left(K_{0.5}^{S}\right)^{n_H}\right)\right) + K \quad (1)$$

where [$S$] is the concentration of variable substrate ($Na^+$ or $P_i$), $I_{Pi}^{\max}$ is the maximum electrogenic activity, $K_{0.5}^{S}$ is the apparent affinity constant for substrate $S$, $n_H$ is the Hill coefficient and $K$ is a constant that take in account of uncoupled leak effects [10]. For $P_i$ activation, the Michaelian form of Eq. 1 was used with $n_H$=1.

Pre-steady state relaxations were recorded using a similar voltage step protocol as for the steady-state assay with steps from $V_h$=−60 or 0 mV, as indicated, to test voltages in the range of −180 to +80 mV in 20 mV increments. The pulse period and period after return to the holding potential was chosen to ensure that relaxations were completed within the recording time window. Signal averaging (typically four-fold) was used to reduce noise. Relaxations were quantified by fitting with one or two component exponential functions unless otherwise noted, commencing the fit approximately 5 ms after the ON or OFF step onset to ensure that endogenous charging components had reached a steady-state. The fits were back-extrapolated to a time point 2 ms after the step onset, at which approximately 90 % of the membrane was charged. The fits were numerically integrated to obtain the charge moved ($Q$) for a step from the holding potential to the test potential. The $Q$–$V$ data were fitted with a Boltzmann function of the form given by:

$$Q = Q_{hyp} + Q_{\max}/1 + \exp(ze(V_{0.5} - V)/kT)) \quad (2)$$

where $V_{0.5}$ is the voltage at which the charge is distributed equally between two hypothetical states, $z$ is the apparent valence of an equivalent charge that moves through the whole of the membrane field, $Q_{\max}$ is the total mobile charge available, $Q_{hyp}$ is the charge of the hyperpolarizing limit and is a function of $V_h$, and $e$, $k$, and $T$ have their usual meanings.

### Determination of activation energy

The Arrhenius equation (e.g., [37]) was used for determining the temperature dependence of the transport kinetics:

$$k_r = A\exp\left(-\frac{E_a}{RT}\right) \quad (3a)$$

where $k_r$ is the reaction rate (substrate-induced current or presteady-state current relaxation rate), $A$ is a constant, $R$ the gas constant, and $E_a$ the activation energy (in kilocalorie per mole). Equation 3a can be recast in a logarithmic form:

$$\ln\ k_r = -(E_a/R)(1/T) + \ln\ A \quad (3b)$$

Linear regression analysis applied to the data plotted as ln $k_r$ vs $1/T$ was used to estimate $E_a$ from the slope.

### $^{32}P$ uptake

Oocytes (6–10 oocytes/group) were first allowed to equilibrate in 100Na solution without tracer. After aspiration of

this solution, oocytes were incubated in 100Na solution containing 1 mM cold $P_i$ and $^{32}P$ (specific activity 10 mCi/mmol $P_i$). Uptake proceeded for 10 min and then oocytes were washed three to four times with ice-cold 100Ch solution containing 2 mM $P_i$, and lysed individually in 10 % SDS for 1 h before addition of scintillation cocktail. The amount of radioactivity taken up by each oocyte was measured by scintillation counting. For temperature-dependence assays, individual oocytes were incubated in the uptake medium and held at the required temperature using a water bath cooling system.

### Simultaneous voltage clamp and fluorometry

The apparatus for simultaneous VCF has been described in detail elsewhere [34, 35]. Cys mutants were labeled in 100Na in presence of MTS-TAMRA (0.4 mM) at room temperature for 4 min. Voltage-dependent changes in fluorescence intensity ($\Delta F$) were determined using a voltage step protocol in which the membrane voltage was stepped from $V_h$=−60 mV to test potentials ranging between −200 and +200 mV in 40 mV increments for a duration of 100–200 ms, and averaged over 20–64 sweeps. Fluorescence signals were analog filtered (eight-pole Bessel) with a low-pass cutoff frequency chosen to optimize the signal-to-noise ratio (typically 500 Hz). $\Delta F$ was measured in 100Ch, XNa (where $X$ represents the [$Na^+$] in millimolar, or 100Na +1$P_i$ (100 mM $Na^+$+1 mM $P_i$); each test substrate concentration application was bracketed with a control solution application (100Na) to allow for correction of a loss of fluorescence. After application of the superfusate, the oocyte was allowed to stabilize in the recording chamber for ~2 min and then fluorescence was recorded. Recordings were baseline corrected relative to the value at $V_h$=−60 mV. The data from single oocytes were corrected for photobleaching and then were normalized to the predicted maximum change in fluorescence ($\Delta F_{max}$) recorded in 100Na and finally pooled. The $\Delta F$–$V$ data were described analytically by fitting with the Boltzmann equation (Eq. 2) to yield the maximum change in fluorescence intensity ($F_{max}$), the midpoint voltage of the $\Delta F$–$V$ distribution ($V_{0.5}^F$) and a slope factor $z^F$.

### Thiol modification by MTS reagents

MTSET (or MTSEA) was prepared from dry stock in water or DMSO to give 1 M stock solution in DMSO, which was kept at −20 °C until required and further diluted with water or DMSO to give 1,000:1 experimental stocks before and adding to 100Na solution to give a final concentration as indicated. MTSET was applied to the recording chamber with gravity feed via a 0.5-mm diameter cannula positioned near the cell. For normal labeling, the incubation time was 3 min and was followed by a 1 min washout period. For determining the apparent accessibility, the superfusion with MTSET was conducted for 1 min followed by washout. During incubation, oocytes were kept at $V_h$=−50 mV unless otherwise noted. After a 1 min washout, the current response to 1 mM $P_i$ at $V_h$=−50 mV was again determined and the MTSET application was repeated. The fixed MTSET concentrations were chosen by pretesting to facilitate determination of the modification rate. The $P_i$-induced current remaining after each successive application of MTS reagent was measured and plotted as a function of the cumulative exposure time, normalized to the initial $P_i$-induced current. The data were fit with a single decaying exponential to determine the effective second order reaction constant using an equation of the form:

$$I_{Pi}{}^t = \left(I_{Pi}{}^0 - I_{Pi}{}^\infty\right)\exp\left(-ctk^*\right) + I_{Pi}{}^\infty \quad (4)$$

where $I_{Pi}{}^t$ is the $P_i$-induced current after a cumulative exposure time $t$, $I_{Pi}{}^0$ is the initial $P_i$-induced current, $I_{Pi}{}^\infty$ is the $P_i$-induced current at $t$=∞, c is the concentration of MTS reagent (assumed to be in excess) and $k$* is the effective second order rate constant, e.g., [22]. For some experiments as indicated, MTSEA was used instead of MTSET and gave the same results.

### Software and data analysis

Simulations of a seven-state model describing electrogenic cotransport were performed using Berkeley Madonna V8.0.2a8 software (www.berkeleymadonna.com). Exponential curve fitting was performed using Clampfit software (Molecular Devices Corp) and subsequent nonlinear regression of data was performed using GraphPad Prism version 3.02/4.02 for Windows (GraphPad Software, San Diego, CA, USA; www.graphpad.com). Data points are shown as mean±SEM. Error bars are not displayed if smaller than symbol.

## Results

### Temperature dependence of steady-state and presteady-state kinetics

To identify partial reactions in the cotransport cycle that determine the unique behavior of AAD-IIc, we measured the temperature dependence of $I_{Pi}$ and presteady-state relaxations. The rationale for these experiments was that if one or more partial reactions were influenced by the mutagenesis, the activation energy may differ from the WT.

At all membrane potentials ($V$) in the test range (−180 mV≤ $V$≤+80 mV), $I_{Pi}$ (100Na, 1 mM $P_i$) showed a strong temperature dependence, whereby it decreased by approximately

60 % for a decrease in temperature from 24 to 20 °C (Fig. 2a). For the electrogenic NaPi-IIa (human isoform), measured under the same conditions, the decrease was typically ≈40 % (data not shown). To quantify the temperature dependence, the $I_{Pi}$–$V$ data were transformed and replotted as Arrhenius plots (see "Methods" section) for test potentials in the range of −180 to −20 mV (Fig. 2b). Data for $V$>−20 mV were too unreliable to fit well and were excluded from analysis. We estimated the activation energy ($E_a$) from the slopes reported by linear regression fitting (Eq. 3b). This showed little dependence on membrane potential and varied from 43±2 kcal$mol^{-1}$ (−180 mV) to 47±6 kcal$mol^{-1}$ (0 mV). In contrast, for the human WT NaPi-IIa, $E_a$ at −180 mV was significantly smaller: (19±4 kcal$mol^{-1}$) and increased to 30±10 kcal$mol^{-1}$ at −20 mV, where there was more experimental uncertainty in the data (Fig. 2c). To establish whether the high $E_a$ for AAD-IIc was caused by the mutations or was an intrinsic property of NaPi-IIc, we performed $^{32}P$ uptake at different temperatures on WT NaPi-IIc expressing oocytes. For these data, the Arrhenius analysis gave $E_a$=13±4 kcal$mol^{-1}$ (*data not shown*).

We next examined the temperature dependence of the presteady-state current relaxations for the AAD-IIc. In the absence of $P_i$ and external interacting cations, voltage steps induce presteady-state currents that reflect charge movements associated with the voltage-dependent reorientation of the unloaded protein alone. In the presence of external $Na^+$ ions, additional charge movement is detected due to $Na^+$ interactions (e.g., [15]). Figure 3a shows example recordings of membrane currents induced by voltage steps recorded from the same oocyte, superfused with 100Na at two temperatures. By reducing the temperature from 26 to 22 °C, the relaxations slowed, which indicated that the underlying process was temperature dependent. We quantified this behavior by fitting the data with a single exponential decay starting 5 ms after the voltage step. For superfusion with 100Na, the ON time constant ($\tau_{ON}$) obtained from fitting relaxations induced by voltage steps from −60 mV to the test potential showed a strong voltage dependence (Fig. 3b) that became more marked at lower temperatures. The OFF time constant ($\tau_{OFF}$) was similarly obtained by fitting relaxations for the corresponding return step to −60 mV. As expected, $\tau_{OFF}$ was independent of the starting potential and the mean values also increased with decreasing temperature and corresponded approximately with the interpolated value at −60 mV for $\tau_{ON}$ (Fig. 3b). The increase in $\tau_{ON}$ and $\tau_{OFF}$ was fully reversible and we confirmed for measurements at 22 and 26 °C that the total charge displaced (see "Methods" section) was unchanged with temperature, as expected (*data not shown*). Resolution of the charge movements at temperatures <20 °C was difficult because of the compromised signal-to-noise ratio and contamination from endogenous currents that depended on the oocyte batch.

As for the steady-state $I_{Pi}$ analysis, the Arrhenius plots for the relaxation rates ($\tau_{ON}^{-1}$ and $\tau_{OFF}^{-1}$) (Fig. 3c) showed a linear dependence on $1/T$. For the $\tau_{ON}^{-1}$ data, there was a small change in the slopes with $V$ and a vertical shift between plots. In contrast, the plots superimposed for $\tau_{OFF}^{-1}$, consistent with the notion that only the target potential determines the relaxation rate, which in this case, was constant (=−60 mV). For superfusion with 100Ch, the predicted $E_a$ obtained from linear regression fits to the Arrhenius plots was ≈40 kcal$mol^{-1}$. There was an upward trend with increasing $V$ and the values were comparable with the $E_a$ determined for $I_{Pi}$. For superfusion with 100Na, the predicted $E_a$ were slightly less than that for $I_{Pi}$ (Fig. 2c) and showed a similar upward trend with $V$.

## Presteady-state relaxations at a fixed temperature

The above findings suggested that partial reactions preceding $P_i$ interaction could account for the temperature dependence of AAD-IIc, We next investigated the presteady-state kinetics in more detail at a fixed temperature (≈22–23 °C) by first focusing on the interaction of $Na^+$ ions with the empty carrier.

We explored the $Na^+$-dependence quantitatively by recording relaxations for equimolar replacement of choline with different [$Na^+$]. Relaxations recorded from a representative oocyte expressing AAD-IIc were similar whether 100 mM $Na^+$ was present in the external medium (100Na) or $Na^+$ was replaced with choline (100Ch; Fig. 4a). To quantify the charge movement, we estimated the charge displacement, by fitting the relaxations with a double exponential function, commencing after completion of the endogenous charging component and integrating the total fit after backward extrapolation ("Methods" section). We found that this fitting procedure described the relaxations better than using a single exponential fit, as judged by the almost complete elimination of residuals (difference between data and fit) as reported by the fitting algorithm over the fitting window. Moreover, we found that by setting the prestep holding potential to 0 mV, we were able to resolve the relaxations over the entire test voltage range without significant contamination from endogenous $Cl^-$ currents. These were usually activated for $V$>0, when stepping from hyperpolarizing potentials and were dependent on the oocyte batch.[1]

For all test solutions, the data showed a characteristic sigmoidal shape (Fig. 4b) that could be described by a Boltzmann function (Eq. 2). The time constants for the

[1] Standard procedures to minimize the contamination by endogenous $Ca^{2+}$-dependent $Cl^-$ currents, such as preincubation of oocytes in BAPTA-AM, or replacement of external $Ca^{2+}$ with $Ba^{2+}$ did not fully suppress these currents.

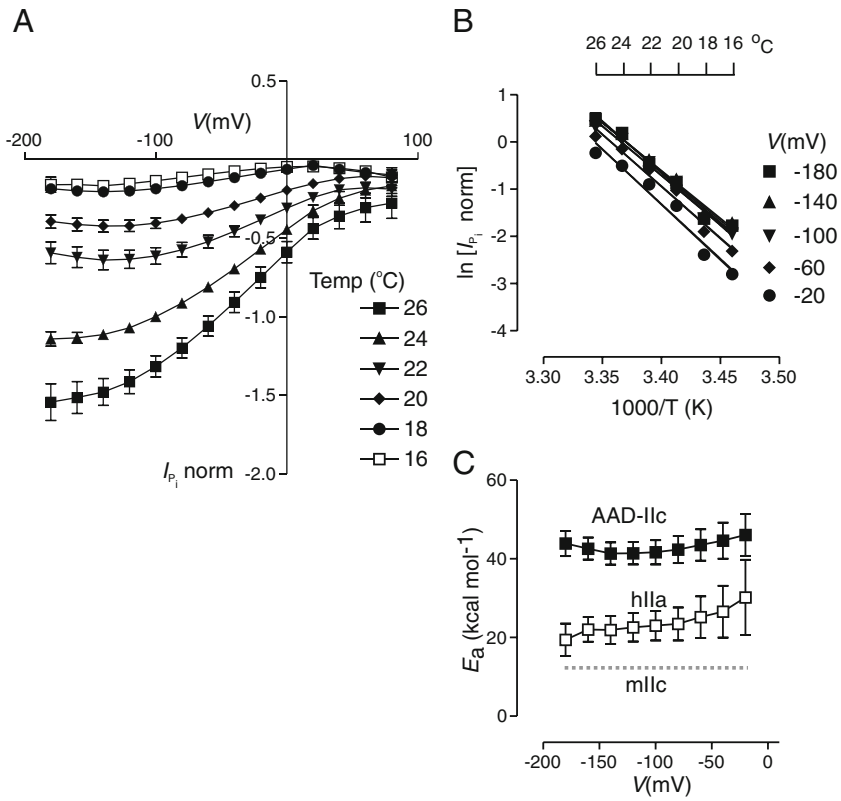


**Fig. 2** Temperature dependence of electrogenic cotransport mediated by AAD-IIc. **a** Current–voltage relationship of $P_i$-induced current ($I_{Pi}$) at different temperatures indicated. Data were normalized to $I_{Pi}$ measured at 24 °C and −100 mV. Data pooled from eight oocytes from two donor animals. Points joined by lines for visualization. **b** Arrhenius plot of AAD-IIc $I_{Pi}$–$V$ data from **a** transformed (see "Materials and methods" section) at selected potentials. Straight lines generated by linear regression analysis. **c** Activation energy ($E_a$) obtained from slope of linear regression fits to Arrhenius plot data for AAD-IIc (*filled squares*) and human NaPi-IIa (hIIa) (*open squares*) plotted as a function of membrane potential. *Dotted line* indicates $E_a$ determined for the electroneutral NaPi-IIc (mouse isoform)

two components ($\tau_1$ and $\tau_2$), plotted as a function of $V$ for different [$Na^+$] showed ≈5-fold difference (for $V$<0 mV) and the slower time constant ($\tau_2$) showed a more obvious voltage dependence with a peak at approximately +30 mV (Fig. 4c). There was also little systematic difference in the magnitude or voltage dependence between the respective time constants in 100Ch or 100Na as well as intermediate [$Na^+$]. This suggested that changing [$Na^+$] did not significantly alter the interactions of external $Na^+$ with AAD-IIc.

The $Q$–$V$ data were fitted with Eq. 2 to obtain the Boltzmann fit parameters ($Q_{max}$, $z$ and $V_{0.5}$) (Fig. 4b). As expected, changing [$Na^+$] did not significantly affect $Q_{max}$ (Fig. 4d) and $z$ was similarly insensitive to [$Na^+$] (Fig. 4e). The mid-point potential ($V_{0.5}$) showed a small depolarizing shift with increasing [$Na^+$] of approximately 30 mV for a tenfold change in [$Na^+$] from 10 to 100 mM (Fig. 4f). For WT human NaPi-IIa and flounder NaPi-IIb, a semilogarithmic plot of $V_{0.5}$ vs [$Na^+$] typically gives a straight line for [$Na^+$]> 10 mM with a slope of 100–120 mV/tenfold [$Na^+$] [2, 33]. Compared with the corresponding data for the electrogenic human NaPi-IIa data [33], the AAD-IIc data were shifted vertically and the linear dependence of $V_{0.5}$ on $\log_{10}$[$Na^+$] was not obvious for the range of [$Na^+$] used (inset, Fig. 4f).

We next investigated the effect of adding 1 mM $P_i$ to the 100Na buffer. Under these conditions, presteady-state relaxations were still visible (Fig. 4a). This differs from the behavior that we have previously reported for WT electrogenic SLC34 proteins, whereby 1 mM $P_i$ strongly suppresses presteady-state charge movements [13, 14, 18]. Moreover, the relaxations for hyperpolarizing steps from the holding potential, $V_h$=−60 mV, indicated that more charge movement was induced in the presence of $P_i$ and this charge then returned during the corresponding OFF step (Fig. 4a, *arrowed*). When $P_i$ was added to 100Ch in the superfusion medium, the presteady-state relaxations were unaffected (data not shown). This confirmed that the presence of $Na^+$ was a prerequisite for $P_i$ interaction with AAD-IIc, consistent with all WT SLC34 isoforms. The results of fitting the corresponding charge movements with Eq. 2, gave $V_{0.5}$=−91±11 mV, $z$=0.51±0.05 and $Q_{max}$ decreased by 18±6 % relative to 100Ch ($n$=5). The main effect of $P_i$ was therefore a hyperpolarizing shift of the equilibrium distribution of mobile charge. We characterized this by determining the dependence of the shift in $V_{0.5}$ on external [$P_i$] (Fig. 5). Figure 5a shows pooled, normalized $Q$–$V$ data ($n$=4) obtained for the ON transition for different [$P_i$] indicated. Increasing [$P_i$] caused a systematic shift of the charge distribution towards hyperpolarizing potentials. As above, the data were fitted with a single Boltzmann function (Eq. 2). For these data, the uncertainties in the Boltzmann fit parameters ($z$, $V_{0.5}$) were reduced by constraining $Q_{max}$ to the value obtained with 0 mM $P_i$. Whereas the predicted $z$ remained reasonably insensitive to changes in [$P_i$] (Fig. 5b), the hyperpolarizing shift of $V_{0.5}$ plotted as a function of [$P_i$] could be well described by fitting with a modified form of Eq. 1 ($n_H$=1; Fig. 5c). This yielded a Michaelis constant ($K_{0.5}^{Pi}$)= 1.5±0.5 mM.

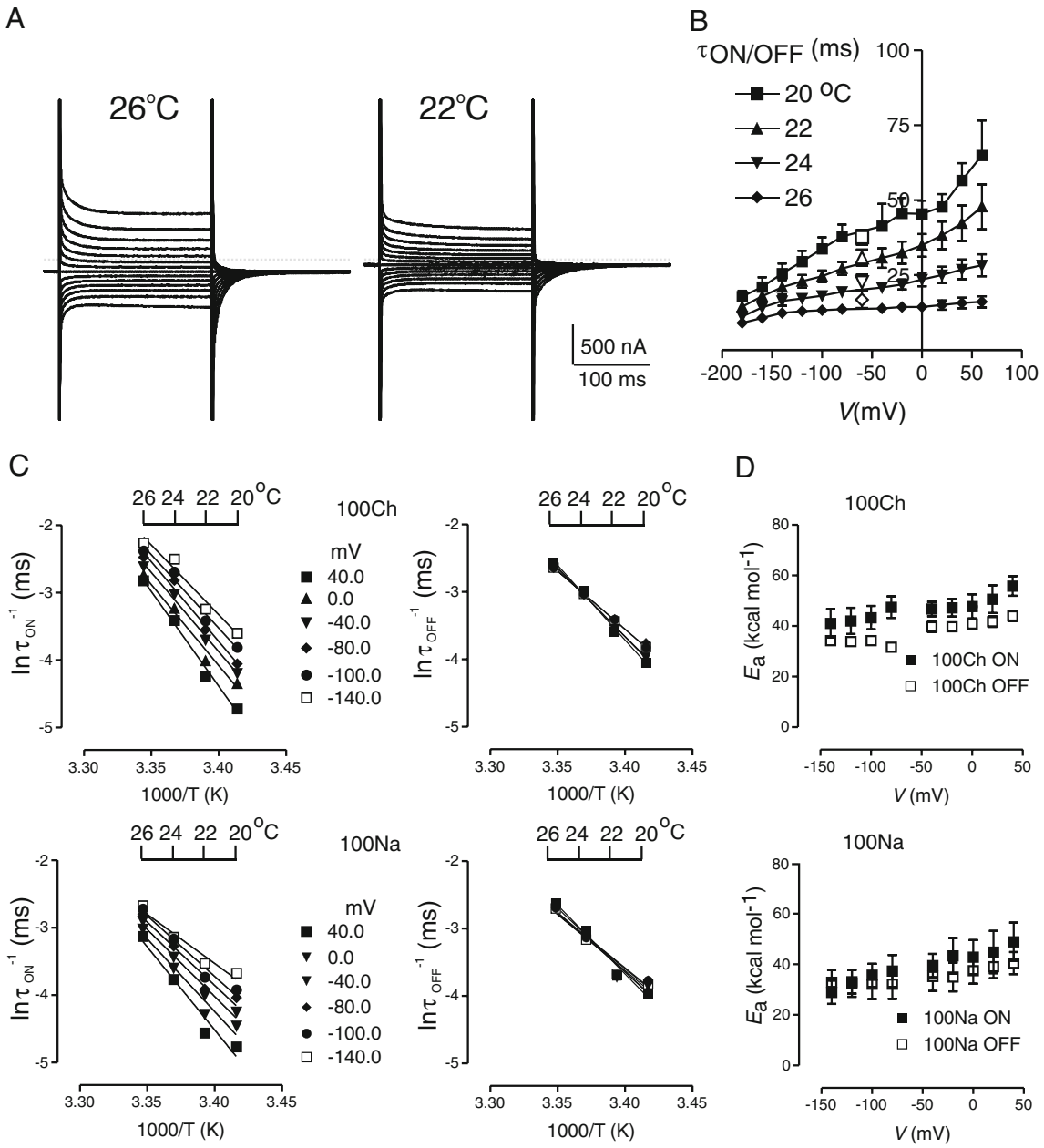


**Fig. 3** Temperature dependence of AAD-IIc presteady-state relaxations. **a** Representative current relaxations recorded from an oocyte expressing AAD-IIc at 26 and 22 °C, superfused in 100Na. Voltage steps shown are from the holding potential of −60 mV to potentials in the range −180 to +80 mV. **b** Relaxation time constant for ON ($\tau_{ON}$, *filled symbols*) and OFF ($\tau_{OFF}$, *open symbols*) steps measured as a function of the test membrane potential for the temperatures indicated ($n$=4). For the OFF relaxations, the data points indicate the mean±SEM of $\tau_{OFF}$ determined from the pooled data at each step. Data points joined for visualization. **c** Arrhenius plots for presteady-state relaxation rate ($\tau_{ON}^{-1}$ and $\tau_{OFF}^{-1}$) for superfusion with 100Ch and 100Na for steps to selected test potentials. Data shown for ON step (from −60 mV holding potential to test potential indicated; *left panels*) and OFF step (from test potential to holding potential; *right panels*). Straight lines are linear regression fits. Data pooled from four oocytes. **d** Activation energies ($E_a$) for the presteady-state relaxation time constants, obtained from slope of linear regression fits to Arrhenius plot data for ON steps (*filled squares*) OFF steps (*open squares*) plotted as a function of membrane potential for the superfusion condition indicated

## Cysteine substitutions in AAD-IIc

Cysteine mutagenesis has proven a useful technique to identify functionally important sites of SLC34 proteins (e.g., [15]. We made Cys substitutions in AAD-IIc and investigated the constructs by means of conventional steady-state kinetics and VCF [7, 19, 20, 34, 35]. We chose sites in AAD-IIc that corresponded to those previously characterized in other SLC34 isoforms (Fig. 6, Table 1). Our rationale was that substitutions at these conserved sites may show similar deviations from WT behavior as found for the AAD-IIc kinetics, and thereby allow us to predict structure-function relationships.

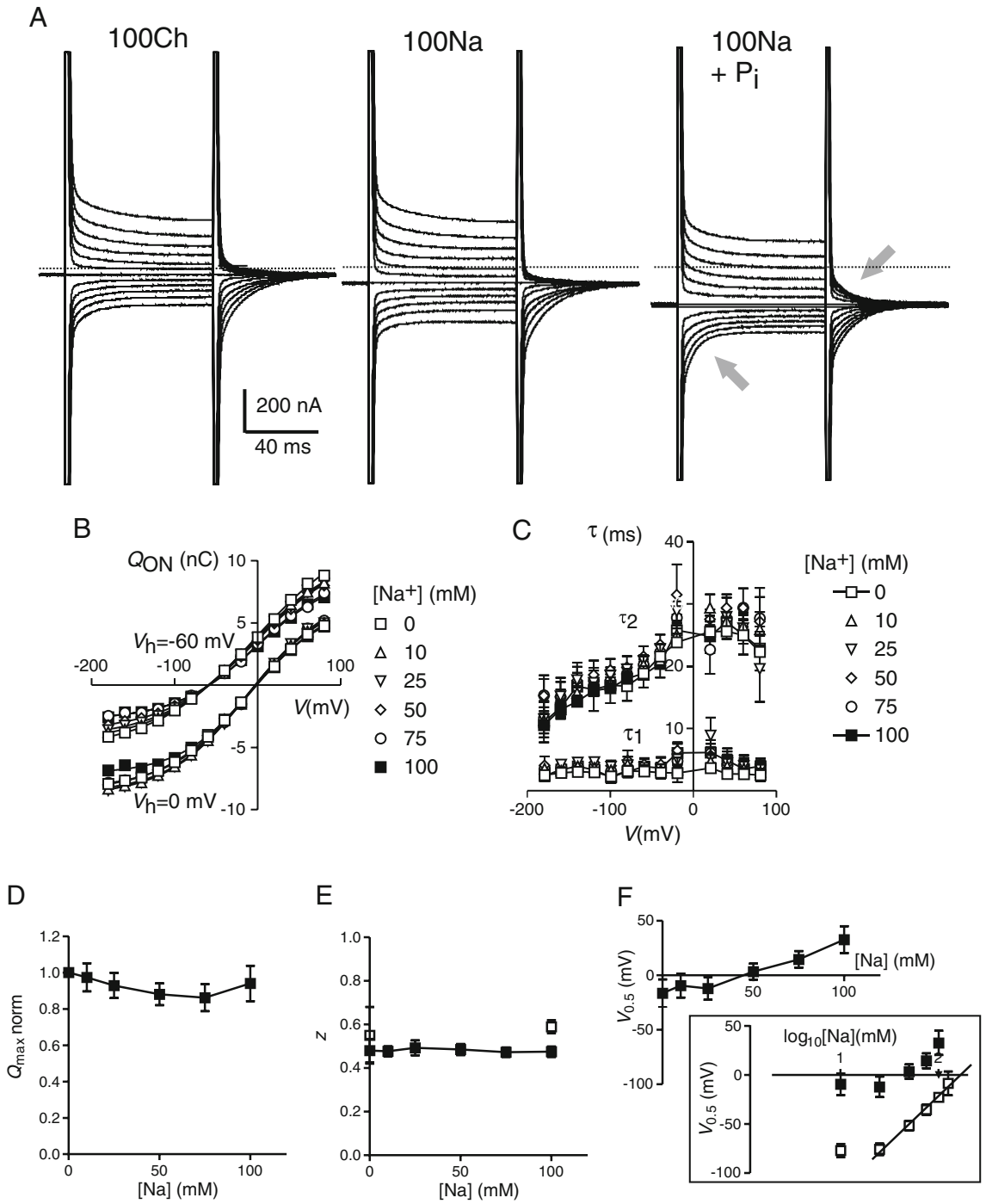


**Fig. 4** Dependence of AAD-IIc presteady-state relaxations on external [$Na^+$]. **a** Presteady-state relaxations recorded in response to voltage steps from a $V_h$=−60 mV to test potentials in the range −160 to +60 mV for three superfusion conditions indicated. *Dotted lines* indicate zero holding current level. For superfusion with 100Na+1$P_i$, the presteady-state relaxations were altered such that more charge movement was induced for steps to and from hyperpolarizing potentials (*arrows*). **b** Typical *Q*–*V* data from a representative oocyte superfused with different [$Na^+$] as indicated, for steps from two holding potentials ($V_h$=0, −60 mV). Data are shown for the ON steps. *Continuous lines* are fits with Eq. 2. **c** Voltage dependence of the two fitted time constants ($\tau_1$, $\tau_2$) for the same superfusion conditions as in **b**. Data pooled from four oocytes. Lines join points corresponding to superfusion with 100Ch and 100Na. **d** Total charge ($Q_{max}$) displaced obtained from Boltzmann fits to data from individual oocytes using Eq. 2 plotted a function of [$Na^+$]. Data were normalized to $Q_{max}$ from 100Ch data set. Data pooled from five cells. **e** Effective valence (*z*) obtained from Boltzmann fits to data from individual oocytes using Eq. 2 plotted as a function of [$Na^+$]. Data pooled from five cells. Open squares are data at 0 and 100 mM $Na^+$ for the human NaPi-IIa from [33]. **f** Midpoint voltage ($V_{0.5}$) from Boltzmann fits to data from individual oocytes using Eq. 2 plotted as a function of [$Na^+$] obtained (*left panel*). Data were replotted on a $\log_{10}$[$Na^+$] scale (*inset*, *filled symbols*). Equivalent data for the human NaPi-IIa are shown (*open symbols*) for comparison (data replotted from [33])

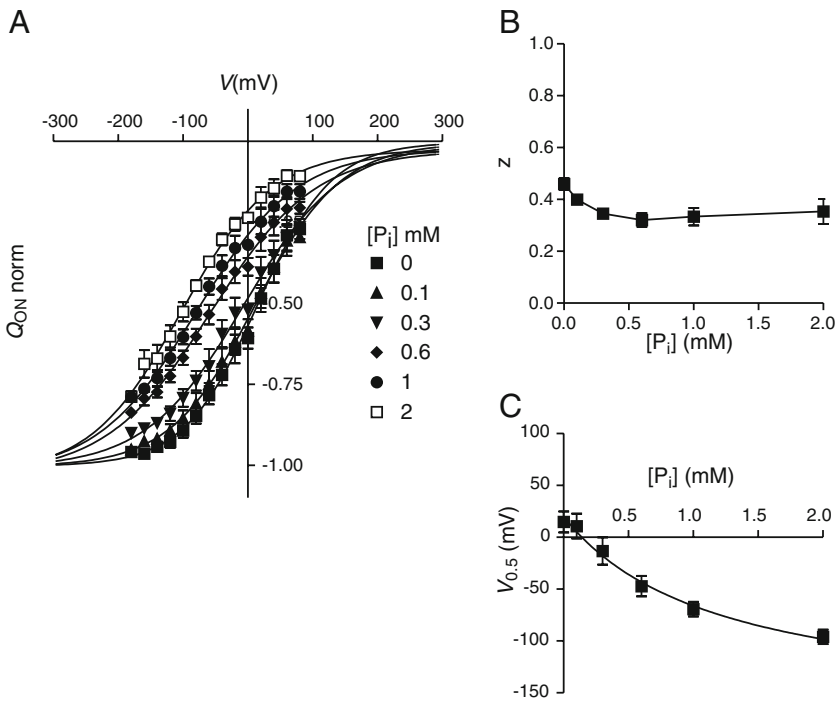


**Fig. 5** Dependence of AAD-IIc presteady-state relaxations on external [$P_i$]. **a** Typical $Q$-$V$ data from a representative oocyte superfused with different [$P_i$] as indicated, for steps from two holding potentials ($V_h$=0, −60 mV). Data are shown for the ON steps. *Continuous lines* are fits with Eq. 2. **b** Effective valence ($z$) obtained from Boltzmann fits to data from individual oocytes, using a modified form of Eq. 1 ($n_H$=1) plotted as a function of [$P_i$]. Data pooled from four cells. **c** Midpoint voltage ($V_{0.5}$) from Boltzmann fits to data from individual oocytes using a modified form of Eq. 1 ($n_H$=1) plotted as a function of [$P_i$] obtained

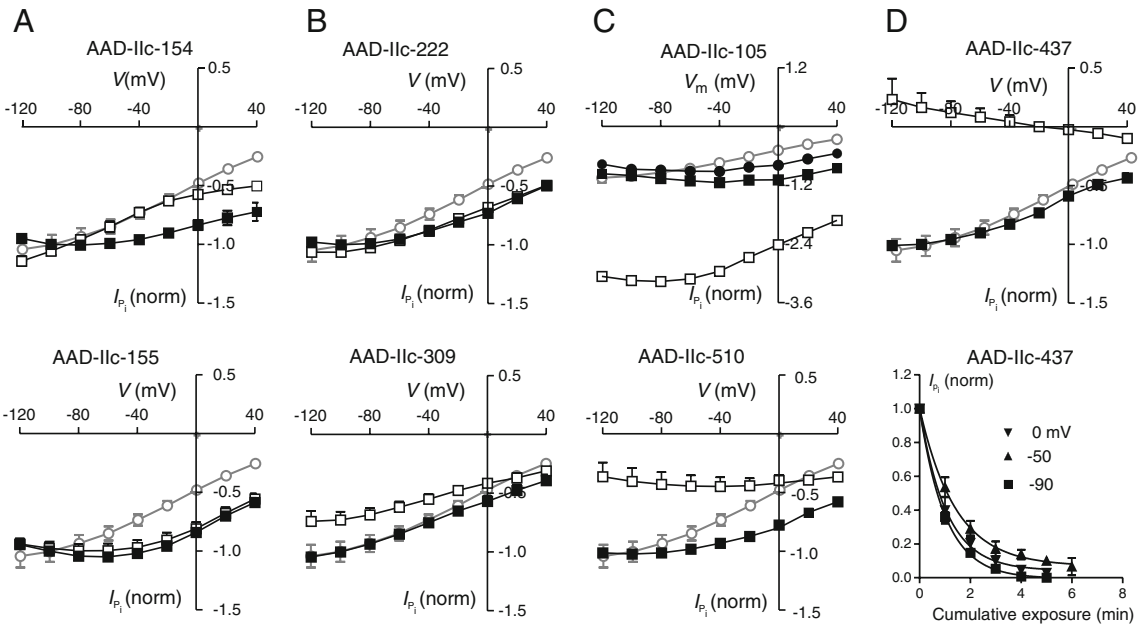


**Fig. 6** Cysteine mutagenesis in the AAD-IIc constructs-dependence of $P_i$-dependent current ($I_{Pi}$) on voltage before and after MTS incubation. After determination of the control $I_{Pi}$ vs V relationship (*filled squares*), oocytes were incubated in 1 mM MTSET for 5 min (*open squares*) and the assay repeated. Data shown normalized to $I_{Pi}$ at −100 mV control condition. Mean±SEM for ≥3 oocytes. *Error bars* smaller than symbol size not shown. Normalized data ($n$=4) for the AAD-IIc are superimposed on each plot for comparison (*gray-filled circles*). **a** For two mutants with adjacent Cys substitutions in the linker between predicted TMD-4 and TMD-5 (Fig. 1b) AAD-IIc-154 (*upper*) showed a hyperpolarizing shift in the voltage dependence of $I_{Pi}$, whereas AAD-IIIc-155 (*lower*) showed no change after MTS incubation. **b** $I_{Pi}$ vs V data for two mutants with Cys substitutions at each end of the large extracellular loop (Fig. 1b), AAD-IIc-222 (*upper*) and AAD-IIc-309 (*lower*). Only AAD-IIc-309 showed a significant change after MTS incubation. **c** $I_{Pi}$ vs V data for Cys mutants AAD-IIc-105 (*upper*) and AAD-IIc-510 (*lower*) that showed reciprocal changes of $I_{Pi}$ after MTS incubation. After MTS modification, one representative AAD-IIc-105 expressing oocyte was exposed to DTT (10 mM, 30 min), which caused a reversion to the initial response (*filled circles*). **d** *Upper* mutant AAD-IIc-437 showed complete suppression of cotransport behavior after MTS incubation with an outward $I_{Pi}$ for hyperpolarizing potentials. *Lower* loss of cotransport activity for mutant AAD-IIc-437 following modification of Cys 437. Normalized response plotted as a function of cumulative exposure time for MTSET (10 μM) exposure with the individual oocytes voltage clamped during incubation to the potential indicated. *Continuous lines* are fits with Eq. 4. See text for more details

**Table 1** Comparison of selected Cys substitution sites among SLC34 isoforms [see Fig. 6]

| | Site of Cys substitution | | | | | | | |
|---|---|---|---|---|---|---|---|---|
| mAAD-IIc | G105 | V154 | S155 | A222 | L309 | S437 | D440 | L510 |
| rNaPi-IIa | G134 [10, 11] | | S183 [30] | | | S460 [24, 25] | E463 [25] | M533 [10, 11] |
| fNaPi-IIb | | S155 [19, 35] | | S226 [34] | Q319 [34] | S448 [19, 35] | | |
| mNaPi-IIc | | | | | | S437 [20] | | |

Blank entry indicates constructs that have not been synthesized or investigated in our laboratory. Equivalent sites indicated according to a multiple sequence alignment for the isoforms and species indicated

*f* flounder, *m* mouse, *r* rat

Before proceeding with the mutagenesis, we first determined if exposure of oocytes expressing AAD-IIc to MTS reagents (MTSET, 1 mM) altered their electrogenic behavior. That no change was observed confirmed that the triple mutation itself had not exposed any previously inaccessible native cysteines that might involved in conformational changes associated with transport function (data not shown). All Cys mutants gave robust $I_{Pi}$, with typical magnitudes of >50 nA at −100 mV. With the exception of AAD-IIc-309, all showed a weak apparent affinity for $P_i$ that is characteristic for AAD-IIc (Table 2). The smaller $P_i$ affinity constant ($K_{0.5}^{Pi}$) for AAD-IIc-309 indicated that this site may be critically associated with $P_i$ interactions. For the other constructs, the $K_{0.5}^{Pi}$ values similar to AAD-IIc and indicated that the Cys substitution had not significantly affected the substrate interactions. In general, the large variation in $K_{0.5}^{P}$ arose from uncertainties in fitting the weakly saturating dose dependence data with Eq. 1. For five of the mutants (AAD-IIc-105, -154,-155,-222, and -510) the Cys substitution weakened the voltage dependence of $I_{Pi}$ compared with AAD-IIc alone, whereas for AAD-IIc-309 and -437 we observed no change in the electrogenic response (Fig. 6).

The effect on $I_{Pi}$ of exposure of oocytes expressing each mutant to MTSET (1 mM for 5 min) depended critically on the site of Cys substitution (Fig. 1b). Mutants fell into two groups: those in which there was no change in the magnitude and voltage dependence of $I_{Pi}$, like AAD-IIc itself, and those that resulted in a marked alteration (Fig. 6, Table 2). We concluded that for the former group the sites of mutagenesis (Ser-155, A-222, and D-440) were either not functionally critical in AAD-IIc, or were not accessible from the external medium. The importance of the site is illustrated in the case of mutations in the predicted re-entrant loop (TMD3,4, Fig. 1b): modification of the Cys substituted at Val-154 caused a significant hyperpolarizing shift in the voltage dependence of $I_{Pi}$ (Fig. 6a, upper panel), whereas the construct AAD-IIc-155 with a Cys substituted at the adjacent Ser showed no detectable change in $I_{Pi}$ after incubation (Fig. 6a, lower panel). Oocytes expressing AAD-IIc with Cys substitution at Ala-222 at one end of the predicted large extracellular loop showed no change in $I_{Pi}$, whereas at the other end (Leu-309) we found a modest ~25 % inhibition in $I_{Pi}$ but with no change voltage dependence (Fig. 6b, lower panel).

Thiol modification of Cys at sites in the two predicted outer linkers (G105 and L510) showed complementary changes in $I_{Pi}$ (Fig. 6c), consistent with previous findings for Cys substituted at the equivalent sites in NaPi-IIa [10]. The voltage dependence of AAD-IIc-105 was weak and after modification $I_{Pi}$ increased fourfold ($V$=−100 mV) to give a voltage dependence that resembled that of AAD-IIc. To verify that this was a direct result of the modification of Cys 105, we exposed oocytes expressing AAD-IIc-105 and prelabeled with MTSEA to the reducing agent DTT. This resulted in a reversion of the electrogenic response close to the original *I–V* relation (Fig. 6c, upper panel). In contrast, AAD-IIc-510 showed the opposite behavior, whereby $I_{Pi}$ was inhibited by ~50 % and after thiol modification, its voltage dependence was similar to AAD-IIc-105 before MTS exposure (Fig. 6c, lower panel).

**Table 2** Summary of properties of Cys mutations in AAD-IIc (see Fig. 6)

| Property | AAD-IIc | +G105C | +V154C | +S155C | +A222C | +L309C | +S437C | +D440C | L510C |
|---|---|---|---|---|---|---|---|---|---|
| $K_{0.5}^{Pi}$–60 mV (mM) | 6.5±4.8 (4) | n.d. | 1.1±0.4 | 2.9±0.8 | 1.5±0.4 | 0.6±0.1 | 1.6±0.4 | 2.0±.8 | 1.5±0.3 |
| $I_{Pi}^{+MTS}/I_{Pi}^{-MTS}$ | ↔ | ↑ | ↓ | ↔ | ↔ | ↓ | ↓ | ↔ | ↓ |
| $\Delta F$ | No | No | Yes | No | Yes | No | Yes | No | No |

↔ indicates that ratio $I_{Pi}^{+MTS}/I_{Pi}^{-MTS}$ remains unchanged, ↑ ratio $I_{Pi}^{+MTS}/I_{Pi}^{-MTS}$ increased, ↓ indicates that ratio $I_{Pi}^{+MTS}/I_{Pi}^{-MTS}$ decreased, *n.d.* not determined

Finally, two mutants involving Cys substitutions at nearby locations in the predicted linker between TMD9 and TMD10 also displayed contrasting behavior. Whereas mutant AAD-IIc-440 showed no resolvable change after incubation (*data not shown*), exposure of oocytes that expressed AAD-IIc-437 to MTS reagents resulted in a significant suppression of $I_{Pi}$ (Fig. 6d, upper panel). For this construct, the typical *I–V* response to 1 mM $P_i$ reversed at −30 mV and displayed a negative slope. This behavior has been previously interpreted to represent full inhibition of cotransport function and recapitulates the behavior of other electrogenic SLC34 isoforms with a Cys at the equivalent site (Table 1, see "Discussion" section) [25, 35]. To quantitate the Cys modification reaction for AAD-IIc-437 and investigate if membrane potential could influence the accessibility of the Cys, we applied MTSET (10 μM) for 1 min intervals at a defined holding potential and measured $I_{Pi}$ at −50 mV after each exposure. The data were fitted with a single decaying exponential function (Eq. 4) to yield the effective pseudo first order rate constants (see "Methods" section): 1.57±0.1 $mM^{-1}s^{-1}$ (0 mV), 1.18±0.03 $mM^{-1}s^{-1}$ (−50 mV), 1.63±0.05 $mM^{-1}s^{-1}$ (−90 mV) ($n$=4; Fig. 6d, lower panel).

## Labeling with MTS-TAMRA and changes in emitted fluorescence intensity

For VCF measurements, we incubated oocytes expressing each of the Cys mutants in a medium containing the fluorophore MTS-TAMRA and tested them for voltage-induced changes in emitted fluorescence intensity under different substrate superfusion conditions (100Na, 100Ch, and 100Na+1$P_i$). Three of the constructs (AAD-IIc-154C, AAD-IIc-222, and AAD-IIc-437) gave measurable $\Delta F$ and were characterized in detail.

*AAD-IIc-437* After labeling with MTS-TAMRA, oocytes expressing AAD-II-437 showed the expected suppressed electrogenic response to 1 mM $P_i$, consistent with the behavior of this mutant when labeled with MTSET (Fig. 6d). We first examined if the steady-state fluorescence was dependent on the superfusate, as we reported for the labeled mutant S437C in NaPi-IIc [20]. Indeed oocytes expressing AAD-IIc-437 and voltage clamped at −60 mV showed up to 3 % reversible quench of $F$ (data not shown), when switching the superfusate from 100Ch to 100Na. All other experiments were performed using a voltage step protocol (see "Methods" section). Representative voltage-induced $\Delta F$ recordings are shown in Fig. 7a. For $V$<0, little or no $\Delta F$ was detected whereas for strongly depolarizing signals $\Delta F$ was quenched in a voltage- and substrate-dependent manner. The quenching was the strongest in the absence of external $Na^+$ (Fig 7b) and at a given $V$, addition of $Na^+$ to the external medium reduced the amount of quenching in a dose-dependent manner. Saturation of the $\Delta F$–$V$ data was not observed at the depolarizing extreme and we were unable to reliably voltage clamp oocytes for $V$>200mV. In the presence of 100 mM $Na^+$, addition of $P_i$ to the external medium reduced the amount of quenching further in a dose-dependent manner (Fig 7a, c).

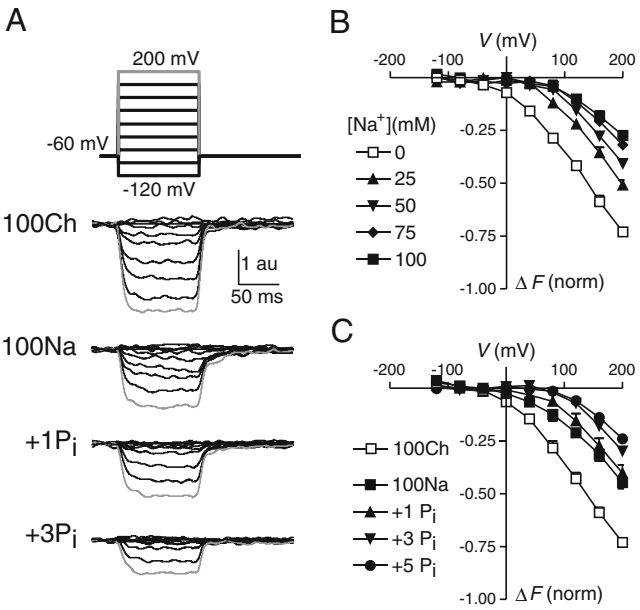


**Fig. 7** VCF recordings from oocytes expressing AAD-IIc-437 and labeled with the fluorophore MTS-TAMRA. **a** Representative VCF recordings from the same oocyte expressing AAD-IIc-437 for the voltage step protocol shown and for the different superfusion conditions indicated. Data traces offset-adjusted to the steady-state fluorescence level at $V_h$=−60 mV. **b** Change in fluorescence ($\Delta F$) plotted as a function of $V$ for oocytes expressing AAD-IIc-437 with external [$Na^+$] varied as indicated. Data for individual oocytes were corrected from photobleaching and loss of fluorescence during the experiment (see "Methods" section) and pooled ($n$=5) by first normalizing to $F_{max}$ predicted from a fit to the 100Ch data using Eq. 2. **c** Change in fluorescence ($\Delta F$) plotted as a function of $V$ oocytes expressing AAD-IIc-437 with external [$P_i$] varied as indicated in the presence of 100 mM $Na^+$. Data from individual oocytes were corrected for photobleaching and loss of fluorescence during the experiment (see "Methods" section) and pooled ($n$=5) by first normalizing to $F_{max}$ predicted from a fit to the 100Ch, 0 mM $P_i$ data using Eq. 2

*AAD-IIc-154* Based on a previous study on the flounder NaPi-IIb isoform [34], we had expected that labeling a Cys substituted at the equivalent site (S155) in AAD-IIc would result in voltage-induced $\Delta F$. Surprisingly, we could not resolve $\Delta F$ from oocytes expressing the construct AAD-IIc-155 (data not shown). However, Cys substitution at the neighboring site (V154) gave a functional construct that exhibited robust $\Delta F$ (Fig. 8a). The voltage step induced $\Delta F$ was similar for superfusion in 100Ch and 100Na; however, the addition of $P_i$ suppressed $\Delta F$ for depolarizing steps and increased $\Delta F$ for hyperpolarizing steps. The $\Delta F$–$V$ data were fit with a single Boltzmann function (Eq. 2, see "Methods" section) to yield

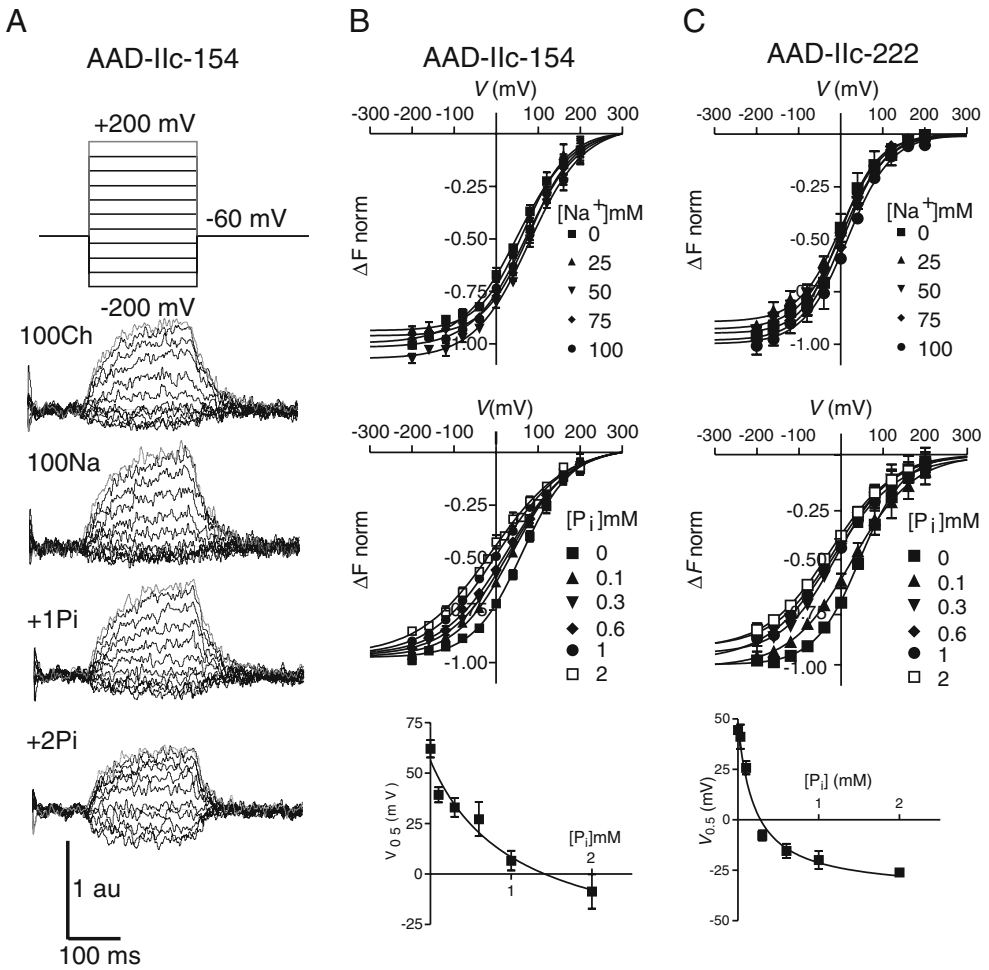


**Fig. 8** VCF recordings from oocytes expressing AAD-IIc-154 and AAD-IIc-222, labeled with the fluorophore MTS-TAMRA. **a** Representative VCF recordings from the same oocyte expressing AAD-IIc-154 for the voltage step protocol shown and the superfusion conditions indicated. All data traces were baseline-adjusted to the steady-state fluorescence level at $V_h$=−60 mV. **b** AAD-IIc-154; *upper* $\Delta F$–$V$ data for different external [$Na^+$]. Data were offset to $\Delta F$ at the depolarizing limit predicted from a fit with Eq. 2 and normalized to $F_{max}$ determined for 100 mM $Na^+$. *Continuous lines* are refits to the adjusted data using Eq. 2. Data pooled from four oocytes. *Center* $\Delta F$–$V$ data for different [$P_i$] in the presence of 100 mM $Na^+$. Data were offset to $\Delta F$ at the depolarizing limit predicted from a fit with Eq. 2 and normalized to $F_{max}$ determined for 0 mM $P_i$. *Continuous lines* are refits to the adjusted data using Eq. 2. Data pooled from four oocytes. *Lower* midpoint voltage ($V_{0.5}$) plotted as a function of [$P_i$] derived from Boltzmann fit. *Continuous line* is fit using a modified form of Eq. 1 ($n_H$=1). **c** AAD-IIc-222; *upper* $\Delta F$–$V$ data for different external [$Na^+$]. Data were offset to $\Delta F$ at the depolarizing limit predicted from a fit with Eq. 2 and normalized to $F_{max}$ determined for 100 mM $Na^+$. *Continuous lines* are refits to the adjusted data using Eq. 2. Data pooled from four oocytes. *Center* $\Delta F$–$V$ data for different [$P_i$] in the presence of 100 mM $Na^+$. Data were offset to $\Delta F$ at the depolarizing limit predicted from a fit with Eq. 2 and normalized to $F_{max}$ determined for 0 mM $P_i$. *Continuous lines* are refits to the adjusted data using Eq. 2. Data pooled from four oocytes. *Lower* midpoint voltage ($V_{0.5}$) plotted as a function of [$P_i$] derived from Boltzmann fit. *Continuous line* is fit using a modified form of Eq. 1 ($n_H$=1)

estimates for the midpoint voltage ($V_{0.5}{}^F$) and slope factor ($z^F$). Unconstrained fits confirmed that $F_{max}$ was largely insensitive to manipulations of the external [$Na^+$] (Fig. 8b, upper). The predicted $V_{0.5}{}^F$ showed a modest increase from +51±9 mV (100Ch) to +71±11 mV (100Na) whereas $z^F$ remained unchanged (0.39±0.06 (100Na) and 0.38±0.05 (100Ch)). We then quantitated the effect of progressively increasing external [$P_i$] (in 100Na; Fig. 8b, center). This resulted in a systematic hyperpolarizing shift in $V_{0.5}{}^F$ (Fig. 8b, lower) together with a reduction in the slope factor $z^F$ from 0.43±0.02 (0 mM $P_i$) to 0.29±0.01 (2 mM $P_i$) ($n$=4). The dependence of $V_{0.5}{}^F$ on [$P_i$] could be described analytically with a modified form of the Michaelis function (Eq. 1 ($n_H$=1) to give an apparent $K_{0.5}{}^{Pi}$=1.04±0.7 mM (Fig. 8b, lower).

*AAD-IIc-222* Oocytes expressing this mutant showed no significant change in electrogenic activity after labeling (Fig. 6b, upper), yet robust $\Delta F$–$V$ was resolved. Like AAD-IIc-154, there was little change in $\Delta F$ when replacing choline with $Na^+$ in the superfusate; however, when $P_i$ (1 or 2 mM ) was added to the superfusate (100Na), $\Delta F$ increased for hyperpolarizing voltage steps and decreased for depolarizing steps relative to

the holding potential, like AAD-IIc-154. The $\Delta F$–$V$ data with variable [$Na^+$] were fit with the Boltzmann function (Eq. 2) (Fig. 8c, upper) and the Boltzmann analysis revealed a small depolarizing shift $V_{0.5}^F$ as [$Na^+$] increased : with 100Ch, $V_{0.5}^F$=−2.2±5.2 mV and at 100Na, $V_{0.5}^F$=+16.0±4.9 mV. In constrast, $F_{max}$ was relatively insensitive to this manipulation and $z^F$ decreased from 0.57±0.06 (100Ch) to 0.48±0.05 (100Na). We also investigated the effect of adding $P_i$ to the 100Na medium (Fig. 8c, center). This caused a hyperpolarizing shift of $V_{0.5}^F$, without significantly affecting $F_{max}$. For this mutant, $V_{0.5}^F$ also showed evidence of saturation at high [$P_i$] and the dependence of $V_{0.5}^F$ on [$P_i$] could be described analytically in terms of a modified form of the Michaelis fit (Eq. 1, $n_H$=1) to give $K_{0.5}^{Pi}$=0.22±0.1mM (Fig. 8c, lower).

## Discussion

For many $Na^+$-coupled solute carriers, transmembrane electrical potential is a source of free energy to drive coupled transport, in addition to the chemical energy imparted by the $Na^+$ concentration gradient. The effect of membrane potential is manifested as the voltage dependence of transport rates (substrate-induced currents) assayed under voltage clamp conditions. Hyperpolarizing membrane potentials increase the inwardly directed transport-associated membrane current and this current correlates directly with solute flux (e.g., [2, 17, 27–29]). Voltage dependence of transport rate implies that there must be one or more partial reactions in the transport cycle whose rate constants are membrane potential dependent. Furthermore, these partial reactions must involve charge displacements that could be either intrinsic to the protein, or arise from the driving cations moving within transmembrane electric field. Such charge displacements are thought to accompany protein conformational changes. It is also possible that the overall transport cycle is electroneutral and one or more partial reactions are voltage dependent and become rate limiting [26], although this not been demonstrated experimentally in the case of SLC34.

For AAD-IIc, which displays three hallmarks of electrogenic SLC34 cotransport (net charge translocation, 3:1 $Na^+/HPO_4^{2-}$ stoichiometry and presteady-state charge displacement), we have proposed that its electrogenicity is a direct result of the re-establishment of the cotranslocation of the $Na^+$ ion associated with transition 1↔2 during the cotransport cycle , as proposed for the WT electrogenic isoforms [4]. Thus, according to our kinetic scheme (Fig. 1a), the salient difference between the electrogenic and electroneutral SLC34 proteins concerns partial reactions between states 0, 1, 2, and 9. This is also supported by the presence of a leak mode for electrogenic SLC34 proteins, that we have hypothesized to involve the translocation of a single $Na^+$ ion per cycle, in the absence of $P_i$ and which can be described kinetically by transitions between these four states [1].[2] In this study, we used AAD-IIc together with mutant constructs involving Cys substitutions at sites previously identified in studies on the electrogenic (NaPi-IIa/b) and electroneutral (NaPi-IIc) to gain new insights into the mechanism of electrogenic cotransport.

### Electrogenicity of the empty carrier imposes an energetic cost to AAD-IIc

Although AAD-IIc displays the qualitative features expected for an electrogenic SLC34 protein, its kinetic characteristics depart significantly from that of the WT electrogenic isoforms, which implied that the mutagenesis altered the kinetics of one or more partial reactions in the cotransport cycle. To identify these reactions, we first examined the temperature dependence of the kinetics of cotransport and cation interactions. Solute coupled carrier proteins generally exhibit a high-temperature dependence that differs significantly from that of ion channels and can be used to distinguish between diffusional processes and those involving conformational changes [3, 5, 6, 21]. With respect to steady-state cotransport rate ($I_{Pi}$), we estimated that $E_a$ for the electrogenic human NaPi-IIa and AAD-IIc was respectively ≈2- and ≈3-fold larger than for the corresponding $P_i$ uptake rate of the electroneutral NaPi-IIc (Fig. 2c). This was clear evidence that cotransporting an additional $Na^+$ ion by the electrogenic isoforms invoked a larger energetic cost. Moreover, our finding that $E_a$ for AAD-IIc was significantly greater than for NaPi-IIa indicated that the mutagenesis in NaPi-IIc had resulted in a less efficient transporter. Given that the cotransport cycle involves a number of partial reactions, one or more of which might be responsible for the overall high $E_a$, we limited the number of possible states the proteins could populate and focused on the temperature dependence of presteady-state relaxations in the absence of $P_i$. In the absence of external $Na^+$ (100Ch) $E_a$ was essentially unchanged (Fig. 3d), we therefore propose that the high $E_a$ of AAD-IIc results from partial reactions that involve neither external $Na^+$ ions nor $P_i$, with the empty carrier (0↔1, Fig. 9a) being the most likely candidate. We cannot explicitly discount the contribution of partial reactions between "inward facing" states, however with low activity of substrates in the cytosol, the probability of occupancy of these states is expected to be concomitantly low. It is therefore most likely that the introduction of the charged Asp-196 into NaPi-IIc has resulted in an electrogenic transition that represents a conformational change between states 0 and 1. This transition is energetically

[2] We also previously reported evidence of a leak mode for AAD-IIc based on the electrogenic response to application of the blocker phosphonoformic acid (PFA) [4]. A detailed characterisation of this mode was not undertaken in the present study due to the low apparent affinity of AAD-IIc for $P_i$ and PFA that would result incomplete suppression of the leak current with the substrate concentrations used.

unfavorable compared to the same transition in the WT electrogenic isoforms [3] and would be expected to involve a concomitantly larger conformational change.

## A seven-state model accounts for the kinetic properties of AAD-IIc

We obtained further insight into the AAD-IIc kinetics, by performing numerical simulations using a set of differential equations that described the rate of change of state occupancy of a reduced form of the 10-state scheme (Fig. 9a). This seven-state scheme allowed us to investigate the steady-state and presteady-state behavior of AAD-IIc with a workable number of free parameters and compare its behavior with corresponding experimental data. We lumped the interactions of $P_i$ and the final $Na^+$ ion before translocation together, but took account of two $Na^+$ ions interacting sequentially before $P_i$ binding and we further simplified the ordered sequence of substrate interactions at the cytoplasmic face by assuming that rapid equilibrium conditions applied to the transitions between states 7 and 9 (Fig. 1a). The simulations successfully predicted the main features of the presteady-state current relaxations (Fig. 9b), namely the weak influence of external $Na^+$ on charge movement and the presence of a significant charge movement in the presence of external $P_i$. For comparison, selected traces from representative data (Fig. 4a) are also shown.

Based on the presteady-state data obtained for AAD-IIc in the absence of external $Na^+$ (100Ch), the effective charge displacement of the empty carrier was the same as in the original model ($0.4e^-$); however, the assignment of voltage dependence to the partial reactions 1↔2 and 9↔0 differed in two respects. First, it was necessary to assign a weaker interaction of the first $Na^+$ ion (1↔2) with the transmembrane electric field (effective valence=$0.1e^-$) to account for: (1) the absence of a strong effect of external [$Na^+$] on the presteady-state charge distribution and the total detectable charge displacement (Figs. 4b and 9c) and (2) the weak hyperpolarizing shift in the midpoint voltage ($V_{0.5}$) of the $Q$–$V$ distribution (Figs. 4f and 9c, lower panel). Second, we increased the effective valence of the partial reaction that accounts for the release of the third $Na^+$ ion on the cytosolic side (9↔0) to $0.5e^-$. Together with a slow backward rate ($Na^+$ release; $k_{09}$=7 $s^{-1}$) and a highly asymmetrical barrier for the transition 0↔9, we could also account for: (1) the increased charge movement for hyperpolarizing steps in the presence of $P_i$ (Figs. 4a and 9b, right panel) and (2) the hyperpolarizing shift in $V_{0.5}$ with increasing [$P_i$] (Figs. 5c and 9d). Moreover, this showed Michaelian behavior (Fig. 9d, lower panel) in accord with the analysis of the experimental data (Fig. 5c) .In the absence of external $P_i$ and the low internal [$Na^+$], the state occupancy is distributed between states 0, 1, and 2. When external $P_i$ is present, state 9 can accumulate after ordered release of 2 $Na^+$ ions and $P_i$ to the cytosol (6→9). The completion of the cotransport cycle only occurs after release of the third $Na^+$ ion, which gives rise to the presteady-state charge movement induced by hyperpolarizing voltage steps (Fig. 9b, right panel) and to a net inward cotransport current in the steady-state.

The most important functional characteristic of AAD-IIc that differed from the WT transporters is the apparent affinity constant for $P_i$ ($K_{0.5}^{Pi}$) that we originally reported to be >100-fold higher than that of either the electrogenic or electroneutral isoforms [4]. This suggested that the triple mutation of NaPi-IIc had specifically affected $P_i$ interactions with the protein. In general, although $K_{0.5}^{Pi}$ can be influenced by all rate constants (forward and backward) associated with partial reactions of the transport cycle, likely candidates could also include those associated with $Na^+$ ion interactions that precede external $P_i$ binding. As expected, our simulations confirmed that $K_{0.5}^{Pi}$ was dependent on the ratio of forward to backward rate constants associated with transitions 1↔2, 2↔3 and 3↔5. However, given the constraints on the model parameters imposed by having good agreement with all the experimental data, we found that partial reaction 3↔5 was indeed the most critical determinant of $K_{0.5}^{Pi}$. Specifically, the ratio $k^0_{12}/k^0_{21}$ was constrained by the dependence of $V_{0.5}$ on external [$Na^+$] [2] and was fixed ≈5 in the simulations to give reasonable agreement with measurement. Furthermore, although altering $k^0_{23}/k^0_{32}$ had little influence on the simulated presteady-state behavior in 0 mM $P_i$, this ratio was also found to be a critical determinant of the apparent affinity constant for $Na^+$ at a given [$P_i$], ($K_{0.5}^{Na)}$, and the cooperativity of Na activation of $I_{Pi}$ [4]. Thus, for AAD-IIc, the low apparent affinity for $P_i$ compared to the electrogenic and electroneutral isoforms most likely results from the effect of the mutagenesis on the $P_i$ binding partial reaction (3↔6) and is largely unaffected by the preceding $Na^+$ interactions. The final set of parameters that gave good agreement with the steady-state data [4] were consistent with a cooperative interaction of two $Na^+$ ions preceding $P_i$ binding ($k^0_{12}/k^0_{21}<k^0_{23}/k^0_{32}$) and with $k^0_{35}/k^0_{53}$ adjusted to give $K_{0.5}^{Pi}$ ≈1 mM and $K_{0.5}^{Na}$ ≈110 mM (at −60 mV; Fig. 9e), similar to previously reported values [4].

In summary, the simulations helped to identify two critical partial reactions that contribute to the AAD-IIc kinetics: (1) the cytosolic release of one $Na^+$ ion from the protein that establishes a rate limiting step in the transport cycle to define the maximum transport rate, and (2) the external $P_i$ interaction which defines the apparent affinity for $P_i$.

## Fluorometric assays complement presteady-state relaxation analysis

The altered kinetic behavior of AAD-IIc compared to the WT proteins indicated that mutagenesis had modified the voltage- and substrate-dependence of the conformational

changes during the transport cycle. To relate these kinetic findings to dynamic changes in the molecular structure, we substituted Cys at sites that previous studies had suggested were involved in unique conformational changes determined by membrane potential and substrate availability [10, 11, 20, 23, 25, 34]. Cys substitution itself was well-tolerated and similar phenotypes were observed after thiol modification, exemplified by mutants AAD-IIc-437, AAD-IIc-105, and AAD-IIc-510.

Exposure of oocytes expressing AAD-IIc-437 to MTS reagents resulted in suppression of cotransport activity, as we have previously reported for the equivalent mutation in other SLC34 isoforms [20, 24, 25, 35] (Fig. 6d). Moreover, the pseudo first-order rate constant for the Cys modification reaction was similar to values we previously reported for modification of a Cys at the equivalent site in rat NaPi-IIa (S460C) [25] and the flounder NaPi-IIb (S448C) [35]. This indicated that external accessibility of this critical site was not changed and moreover, the accessibility was also insensitive to membrane potential ($V \leq 0$ mV). The voltage dependence of mutants AAD-IIc-105 and AAD-IIc-510 (Fig. 6c) also showed qualitatively similar behavior as previously reported for the equivalent Cys substitutions in the rat NaPi-IIa [11] whereby Cys modification resulted in a complementary change in the voltage dependence. These findings not only confirmed that AAD-IIc has a similar topology to NaPi-IIa at these critical sites, but that the functional consequences of Cys modification at these sites were comparable.

The substituted Cys were labeled with fluorophores to act as reporters of local conformational changes [19, 20, 34, 35]. The behavior of labeled oocytes expressing AAD-IIc-437 in response to changing the superfusate from 100Na to 100Ch was qualitatively the same as we previously reported for the NaPi-IIc mutant S437C [20]: in the steady-state ($V_h$=−60 mV), addition of $Na^+$ quenched the fluorescence. However, the response of AAD-IIc-437 to voltage steps differed from the electrogenic NaPi-IIb mutant S448C [35], whereby under all superfusion conditions there was resolvable voltage-induced change in fluorescence intensity ($\Delta F$) *only* for depolarizing voltage steps (Fig. 7). Superfusion with 100Ch gave the largest quench of $\Delta F$ at a given positive test potential and this diminished in a concentration-dependent manner with the addition of more external $Na^+$ as well as with the addition of external $P_i$. In contrast, for the electrogenic S448C mutant in flounder NaPi-IIb [35], no resolvable $\Delta F$ was reported for voltage steps from −60 mV to test potentials >0 mV, and increasing external [$Na^+$] quenched $\Delta F$ for hyperpolarizing potentials. Similarly, for S437C mutant made in the mouse NaPi-IIc we reported that the addition of external $Na^+$ caused a quenching of the steady-state fluorescence [20] as we also observed for the steady-state $F$ reported by AAD-IIc-437.

One interpretation of the behavior of AAD-IIc-437 is that the microenvironment of the fluorophore at site 437 reports

**Fig. 9** Simulations using a reduced seven-state model recapitulate AAD-IIc kinetic behavior. **a** Reduced seven-state model used for AAD-IIc simulations. *Boxed values* indicate effective valence associated with partial reactions representing empty carrier and $Na^+$ interactions and should be compared with the equivalent for the WT electrogenic transport cycle (Fig. 1a). Transition (2↔9) accounts for uncoupled $Na^+$-leak (see [1]). The voltage dependence of these partial reactions was modeled by applying Eyring transition state theory to describe the dependence of transition rate constants on membrane potential. The voltage-dependent partial reactions involve the movement of the equivalent lumped charges that result in a conformational state change by crossing a sharp energy barrier. We assumed symmetrical barriers, except for transition 9↔0 where an asymmetry factor (asf=0.15) was used to improve agreement with experimental data. The rate constants (in per second) were as follows: $-k_{10}=40\exp(-Vz_{10}\mu/2)$, $k_{01}=40\exp(Vz_{10}\mu/2)$; $k_{12}=[\mathrm{Na}]_0$ $5{,}000\exp(-Vz_{12}\ \mu/2)$, $k_{21}=1{,}200\exp(Vz_{12}\ \mu/2)$, $k_{23}=[\mathrm{Na}]_0$ 5,000, $k_{32}=400$, $k_{35}=[\mathrm{Na}]_0$ $[P_i]_0 2{,}000$, $k_{53}=100$, $k_{56}=k_{65}=10$, $k_{69}=10^4$, $k_{29}=1$, $k_{09}=[\mathrm{Na}]_i 200\exp(Vz_{09}\ \mu\times\mathrm{asf})$, $k_{90}=7\exp(-Vz_{09}\ \mu(1-\mathrm{asf}))$ and $\mu=e/kT\approx 40\ V^{-1}$ at 20 °C, $z_{10}=0.4$, $z_{12}=0.1$,$z_{09}=0.5$. The rates constants $k_{96}$, $k_{92}$ were defined independently in terms of the other rate constants under conditions of zero driving force to satisfy the detailed balance for the leak and cotransport cycles. We assumed the following substrate concentrations on the cytosolic side: $[\mathrm{Na}]_i$=10 mM and $[P_i]_i$=1 μM. **b** Simulations of presteady-state currents in response to voltage steps from −60 mV to test potentials as indicated for three superfusion conditions. In each case, baseline correction has been made. To obtain the true relaxation current magnitude (in **b**), traces should be scaled by $N_t e$, where $N_t$ is the number of transporters and $e$=the electronic charge. For each case, the corresponding traces from the representative oocyte (Fig. 4a) are shown (*boxed*) for test potentials to −180 and +80 mV with the endogenous oocyte charging transients removed by curve fitting. The measured data were scaled vertically to give a reasonable match to the simulated data. **c** *Upper* normalized $Q$–$V$ data for $Na^+$ interaction with external $P_i$=0. *Continuous lines* are fits to data using Eq. 2 with all parameters unconstrained. $Q$–$V$ data were normalized to $Q_{max}$ obtained from fit to the data set for 100 mM $Na^+$. *Lower* dependence $V_{0.5}$ on [$Na^+$]. This should be compared with Fig. 4f. **d** *Upper* normalized $Q$–$V$ data for $P_i$ interaction with external [$Na^+$]=100 mM. *Continuous lines* are fits to data using Eq. 2 with all parameters unconstrained. $Q$–$V$ data were normalized to $Q_{max}$ obtained from fit to 0 mM $P_i$ data set. *Lower* Dependence of $V_{0.5}$) on [$P_i$]. This should be compared with Fig. 5c. *Continuous line* is a fit using a modified form of Eq. 1 ($n_H$=1), giving $K_{0.5}^{Pi}$=1 mM. **e** Simulated steady-state $P_i$ activation (−60 mV, 100 mM $Na^+$; *filled symbols*) and $Na^+$ activation (−60 mV, 1 mM $P_i$; *open symbols*) using data set in **b**. The apparent affinity constants under these conditions were $K_{0.5}^{Pi}$=1.05 mM and $K_{0.5}^{Na}$=102 mM and the Hill coeff ($n_H$)=2.4, for $Na^+$ activation found by fitting simulated data points with Eq. 1. Data should be scaled by $N_t e$ to obtain the $P_i$-induced current

$Na^+$ interactions from *either* side of the membrane, depending on the membrane potential and availability of $Na^+$ ions. This would be consistent with the alternating access mechanism for cation driven transport (e.g., [12]). Thus, for strongly depolarizing voltage steps, and *no* external $Na^+$, cytosolic $Na^+$ ions would be driven to their binding site (partial reaction 0→9), thus giving rise to $\Delta F$ when superfusing with external 100Ch (Fig. 6b). As fluorescent quenching is thought to result from exposure of the fluorophore to a hydrophilic environment (e.g., [8]), this behavior would suggest that this site becomes more exposed to the cytosol as *internal* $Na^+$ ions bind to the protein. By

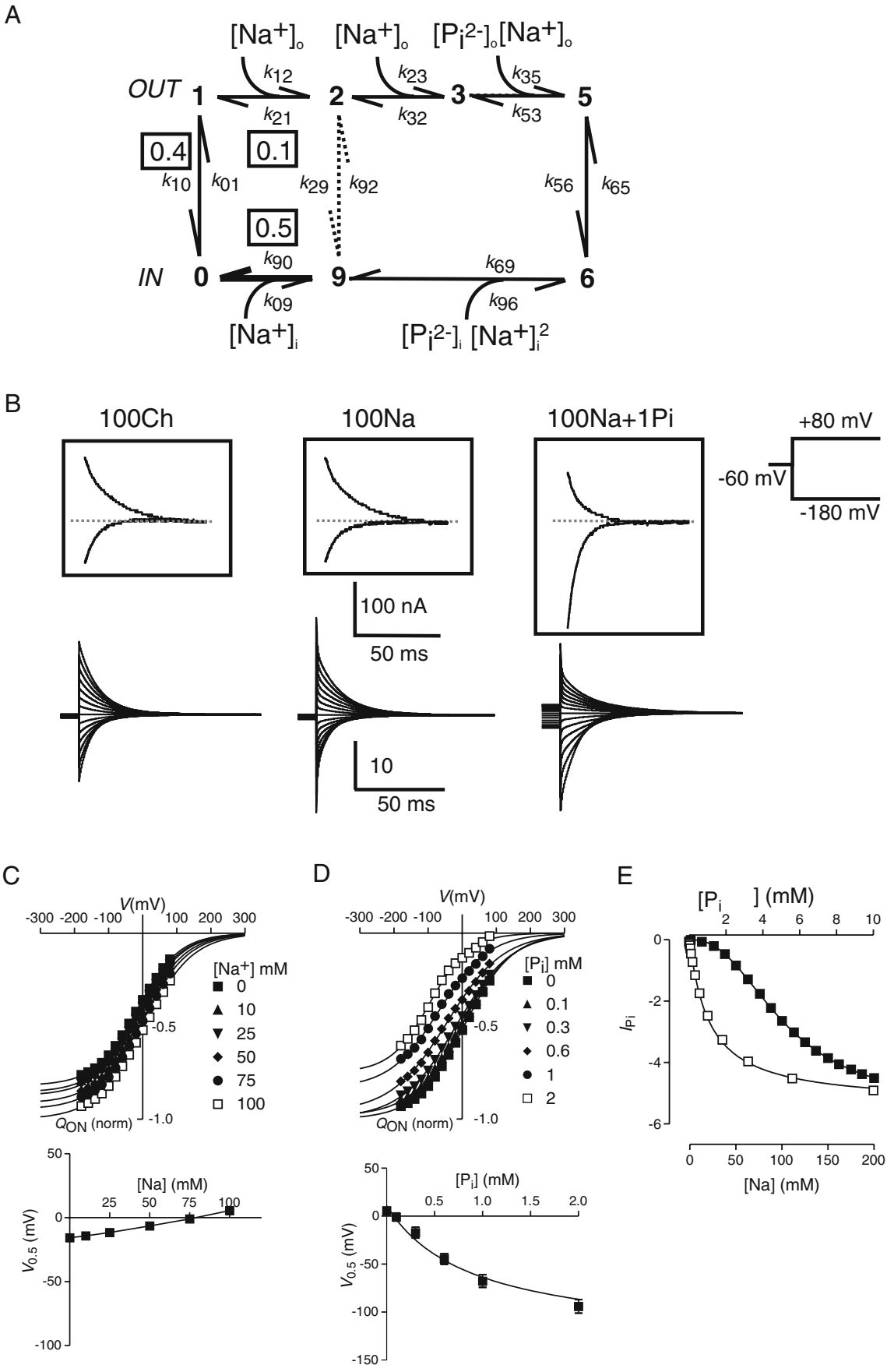
A
[Na+]o
[Na+]o
[Pi2-]o[Na+]o
k12
k23
k35
OUT
1
2
3
5
k21
k32
k53
0.4
0.1
k10
k01
k29
k92
k56
k65
0.5
k90
k69
IN
0
9
6
k09
k96
[Na+]i
[Pi2-]i [Na+]i2
B
100Ch
100Na
100Na+1Pi
+80 mV
-60 mV
-180 mV
100 nA
50 ms
10
50 ms
C
V(mV)
-300 -200 -100 100 200 300
[Na+] mM
0
10
25
50
75
100
-0.5
-1.0
QON (norm)
50
0
-50
-100
[Na] (mM)
25 50 75 100
V0.5 (mV)
D
V(mV)
-300 -200 -100 100 200 300
[Pi] mM
0
0.1
0.3
0.6
1
2
-0.5
-1.0
QON (norm)
50
0
-50
-100
-150
[Pi] (mM)
0.5 1.0 1.5 2.0
V0.5 (mV)
E
[Pi ] (mM)
2 4 6 8 10
0
-2
-4
-6
IPi
0 50 100 150 200
[Na] (mM)

increasing *external* [$Na^+$], the state distribution of AAD-IIc would be altered to favor states 1 and 2 (external binding of $Na^+$) with little voltage-dependent conformational change when external $Na^+$ binds, consistent with our presteady-state relaxation findings. Under these conditions, site 437 would become exposed to the external medium and thereby account for the quenching of steady-state fluorescence in the presence of external $Na^+$. The addition of external $P_i$ (in the presence of external $Na^+$) would further diminish the effect of the cytosolic $Na^+$ interaction on $\Delta F$, as the transport cycle proceeds in the forward (clockwise direction, Fig. 9a). That we did not observe $\Delta F$ for depolarizing voltage steps with the S448C flounder NaPi-IIb mutant [35] suggests that for the WT electrogenic isoforms, the conformational changes associated with the binding and release of the last $Na^+$ ion to the cytosol (9↔0) are small compared to AAD-IIc. This is also supported by the model prediction, whereby this $Na^+$ ion would move through a smaller fraction of the transmembrane electric field (Fig. 9a).

The other two AAD-IIc Cys mutants from which we could detect fluorescence changes (AAD-IIc-154, AAD-IIc-222) showed behavior consistent with the altered kinetics of AAD-IIc. The $\Delta F$ reported by a fluorophore linked to the Cys −154 (AAD-IIc-154) can be compared with that for the equivalent mutant in flounder NaPi-IIb (S155C) [34]. This mutant shows strong dependence of $\Delta F$ on external [$Na^+$] (slope of $V_{0.5}$ vs log [$Na^+$]=140 mV/decade), unlike the weak dependence we report here for AAD-IIc-154 (Fig. 8a, b). Moreover, for S155C when external [$P_i$] is changed in the presence of 100 mM $Na^+$, we observe strong quenching, but no obvious shift in $V_{0.5}{}^{F}$, whereas AAD-IIc-154 showed a hyperpolarizing shift (Fig. 8b) that was qualitatively similar to the shift found for presteady-state relaxations with variable [$P_i$] (Fig. 5c) and comparable to the transport $K_{0.5}{}^{Pi}$ (Table 1). The insensitivity to changes in external [$Na^+$] for AAD-IIc-154 indeed suggested that the microenvironment of the fluorophore at Cys −154 reports similar conformational changes to those that give rise to the presteady-state charge movement: reorientation of the empty carrier, including the release of the final $Na^+$ ion to the cytosol during cotransport. Qualitatively similar behavior was found for the $\Delta F$–$V$ data obtained by labeling mutant AAD-IIc-222. Taken together, these findings suggest that the local environments of these sites undergo voltage-dependent conformational changes associated with the empty carrier and cytosolic $Na^+$ release.

## Conclusions

Electrogenicity can be conferred to the electroneutral $Na^+$-coupled $P_i$ cotransporter (NaPi-IIc) by the substitution of three amino acids, one of which is negatively charged (D195). We hypothesize that the movement of this charge (evidenced by presteady-state relaxations), results in a conformational change of the empty carrier between inward and outward facing orientations (evidenced by fluorometric recordings), that allows a single $Na^+$ ion to bind from either side of the membrane, subsequently translocate and dissociate, driven by the electrochemical gradient for $Na^+$. Whether or not this charge itself is part of the cation coordination or indirectly exposes a binding site cannot be determined without 3-D structural information. Certainly, for this charged residue to fulfill the role as the empty carrier "voltage sensor", the current secondary topology model of SLC34 proteins [15], which places D195 close to the cytosolic end of TMD5 and effectively outside the transmembrane electric field (Fig. 1b), would require reassessment.

Although AAD-IIc can be considered an "imperfect" transporter, with a significantly greater $E_a$ than the WT electroneutral and electrogenic isoforms, its deviation from WT behavior has revealed an important partial reaction in the physiologically relevant transport cycle, namely the cytosolic release of a $Na^+$ ion prior to reorientation of the empty carrier. For AAD-IIc, the kinetics of this transition impose a rate-limiting step on the transport cycle, consistent with this ion being more tightly bound to AAD-IIc than for the electrogenic WT isoforms. Identification of this partial reaction in the electrogenic WT would otherwise be difficult to achieve experimentally using the intact oocyte system. The cytosolic dissociation of this $Na^+$ ion, revealed through mutagenesis, means that AAD-IIc provides a unique tool to investigate cation interactions at the internal protein interface for SLC34 proteins.

We originally identified three critical regions in the SLC34 sequences that differed significantly between electrogenic and electroneutral isoforms [4]. Although one of these regions contains D195 (or its equivalent) found in the electrogenic isoforms, the roles played by other dissimilar polar and nonpolar residues in the other regions in establishing a voltage-dependent interaction of external $Na^+$ ions, together with the high apparent affinity for $P_i$, remain to be elucidated.

**Acknowledgments** We gratefully acknowledge Eva Hänsenberger for oocyte preparation. Special thanks to Dr Anne-Kristine Meinild (UZH) and Dr Donald D.F. Loo (UCLA) for their insightful comments. This work was supported by the Swiss National Science Foundation grant to ICF and Hartmann Müller-Stiftung grant to CG.

## References

1. Andrini O, Ghezzi C, Murer H, Forster IC (2008) The leak mode of type II Na(+)-P(i) cotransporters. Channels (Austin) 2:346–357
2. Andrini O, Meinild AK, Ghezzi C, Murer H, Forster IC (2012) Lithium interactions with $Na^+$-coupled inorganic phosphate cotransporters: insights into the mechanism of sequential cation binding. Am J Physiol Cell Physiol 302:C539–554

3. Bacconi A, Ravera S, Virkki LV, Murer H, Forster IC (2007) Temperature-dependency of steady-state and presteady-state kinetics of a type IIb $Na^+/P_i$ cotransporter. J Mem Bio 215(2–3):81–92
4. Bacconi A, Virkki LV, Biber J, Murer H, Forster IC (2005) Renouncing electrogenicity is not free of charge: switching on electrogenicity in a $Na^+$-coupled phosphate cotransporter. Proc Natl Acad Sci U S A 102:12606–12611
5. Binda F, Bossi E, Giovannardi S, Forlani G, Peres A (2002) Temperature effects on the presteady-state and transport-associated currents of GABA cotransporter rGAT1. FEBS Lett 512:303–307
6. Bossi E, Cherubino F, Margheritis E, Oyadeyi AS, Vollero A, Peres A (2012) Temperature effects on the kinetic properties of the rabbit intestinal oligopeptide cotransporter PepT1. Pflugers Arch 464:183–191
7. Breusegem SY, Takahashi H, Giral-Arnal H, Wang X, Jiang T, Verlander JW, Wilson P, Miyazaki-Anzai S, Sutherland E, Caldas Y, Blaine JT, Segawa H, Miyamoto K, Barry NP, Levi M (2009) Differential regulation of the renal sodium-phosphate cotransporters NaPi-IIa, NaPi-IIc, and PiT-2 in dietary potassium deficiency. Am J Physiol Renal Physiol 297:F350–361
8. Cha A, Bezanilla F (1998) Structural implications of fluorescence quenching in the Shaker $K^+$ channel. J Gen Physiol 112:391–408
9. de la Horra C, Hernando N, Lambert G, Forster I, Biber J, Murer H (2000) Molecular determinants of pH sensitivity of the type IIa Na/P(i) cotransporter. J Biol Chem 275:6284–6287
10. Ehnes C, Forster IC, Bacconi A, Kohler K, Biber J, Murer H (2004) Structure-function relations of the first and fourth extracellular linkers of the type IIa $Na^+/P_i$ cotransporter: II Substrate interaction and voltage dependency of two functionally important sites. J Gen Physiol 124:489–503
11. Ehnes C, Forster IC, Kohler K, Bacconi A, Stange G, Biber J, Murer H (2004) Structure-function relations of the first and fourth predicted extracellular linkers of the type IIa $Na^+$/Pi cotransporter: I Cysteine scanning mutagenesis. J Gen Physiol 124:475–488
12. Forrest LR, Kramer R, Ziegler C (2011) The structural basis of secondary active transport mechanisms. Biochim Biophys Acta 1807:167–188
13. Forster I, Hernando N, Biber J, Murer H (1998) The voltage dependence of a cloned mammalian renal type II $Na^+/P_i$ cotransporter (NaPi-2). J Gen Physiol 112:1–18
14. Forster IC, Biber J, Murer H (2000) Proton-sensitive transitions of renal type II $Na^+$-coupled phosphate cotransporter kinetics. Biophys J 79:215–230
15. Forster IC, Hernando N, Biber J, Murer H (2012) Phosphate transport kinetics and structure–function relationships of SLC34 and SLC20 proteins. Curr Top Membr 70:313–356
16. Forster IC, Kohler K, Biber J, Murer H (2002) Forging the link between structure and function of electrogenic cotransporters: the renal type IIa $Na^+/P_i$ cotransporter as a case study. Prog Biophys Mol Biol 80:69–108
17. Forster IC, Loo DD, Eskandari S (1999) Stoichiometry and $Na^+$ binding cooperativity of rat and flounder renal type II $Na^+$-$P_i$ cotransporters. Am J Physiol 276:F644–649
18. Forster IC, Wagner CA, Busch AE, Lang F, Biber J, Hernando N, Murer H, Werner A (1997) Electrophysiological characterization of the flounder type II $Na^+/P_i$ cotransporter (NaPi-5) expressed in *Xenopus laevis* oocytes. J Membr Biol 160:9–25
19. Ghezzi C, Meinild AK, Murer H, Forster IC (2011) Voltage- and substrate-dependent interactions between sites in putative reentrant domains of a Na(+)-coupled phosphate cotransporter. Pflugers Arch 461:645–663
20. Ghezzi C, Murer H, Forster IC (2009) Substrate interactions of the electroneutral $Na^+$-coupled inorganic phosphate cotransporter (NaPi-IIc). J Physiol 587:4293–4307
21. Hazama A, Loo DD, Wright EM (1997) Presteady-state currents of the rabbit Na+/glucose cotransporter (SGLT1). J Membr Biol 155:175–186
22. Karlin A, Akabas MH (1998) Substituted-cysteine accessibility method. Methods Enzymol 293:123–145
23. Lambert G, Forster IC, Biber J, Murer H (2000) Cysteine residues and the structure of the rat renal proximal tubular type II sodium phosphate cotransporter (rat NaPi IIa). J Membr Biol 176:133–141
24. Lambert G, Forster IC, Stange G, Biber J, Murer H (1999) Properties of the mutant Ser-460-Cys implicate this site in a functionally important region of the type IIa $Na^+/P_i$ cotransporter protein. J Gen Physiol 114:637–652
25. Lambert G, Forster IC, Stange G, Kohler K, Biber J, Murer H (2001) Cysteine mutagenesis reveals novel structure-function features within the predicted third extracellular loop of the type IIa $Na^+/P_i$ cotransporter. J Gen Physiol 117:533–546
26. Lester HA, Mager S, Quick MW, Corey JL (1994) Permeation properties of neurotransmitter transporters. Annu Rev Pharmacol Toxicol 34:219–249
27. Mackenzie B, Loo DD, Wright EM (1998) Relationships between Na+/glucose cotransporter (SGLT1) currents and fluxes. J Membr Biol 162:101–106
28. Matthews E Jr, Rahnama-Vaghef A, Eskandari S (2009) Inhibitors of the gamma-aminobutyric acid transporter 1 (GAT1) do not reveal a channel mode of conduction. Neurochem Int 55:732–740
29. Meinild AK, Forster IC (2012) Using lithium to probe sequential cation interactions with GAT1. Am J Physiol Cell Physiol 302: C1661–1675
30. Radanovic T, Gisler SM, Biber J, Murer H (2006) Topology of the type IIa Na+/P(i) cotransporter. J Membr Biol 212:41–49
31. Segawa H, Kaneko I, Takahashi A, Kuwahata M, Ito M, Ohkido I, Tatsumi S, Miyamoto K (2002) Growth-related renal type II Na/Pi cotransporter. J Biol Chem 277:19665–19672
32. Virkki LV, Forster IC, Bacconi A, Biber J, Murer H (2005) Functionally important residues in the predicted 3rd transmembrane domain of the type IIa sodium-phosphate co-transporter (NaPi-IIa). J Membr Biol 206:227–238
33. Virkki LV, Forster IC, Biber J, Murer H (2005) Substrate interactions in the human type IIa sodium-phosphate cotransporter (NaPi-IIa). Am J Physiol 288:F969–F981
34. Virkki LV, Murer H, Forster IC (2006) Mapping conformational changes of the type IIb $Na^+/P_i$ cotransporter by voltage clamp fluorometry. J Biol Chem 281:28837–28849
35. Virkki LV, Murer H, Forster IC (2006) Voltage clamp fluorometric measurements on a type II $Na^+$-coupled $P_i$ cotransporter: shedding light on substrate binding order. J Gen Physiol 127:539–555
36. Werner A, Kinne RK (2001) Evolution of the Na-$P_i$ cotransport systems. Am J Physiol 280:R301–312
37. Winzor DJ, Jackson CM (2006) Interpretation of the temperature dependence of equilibrium and rate constants. J Mol Recognit 19:389–407